Cell

Structural insights into the human D1 and D2 dopamine receptor signaling complexes

Graphical Abstract

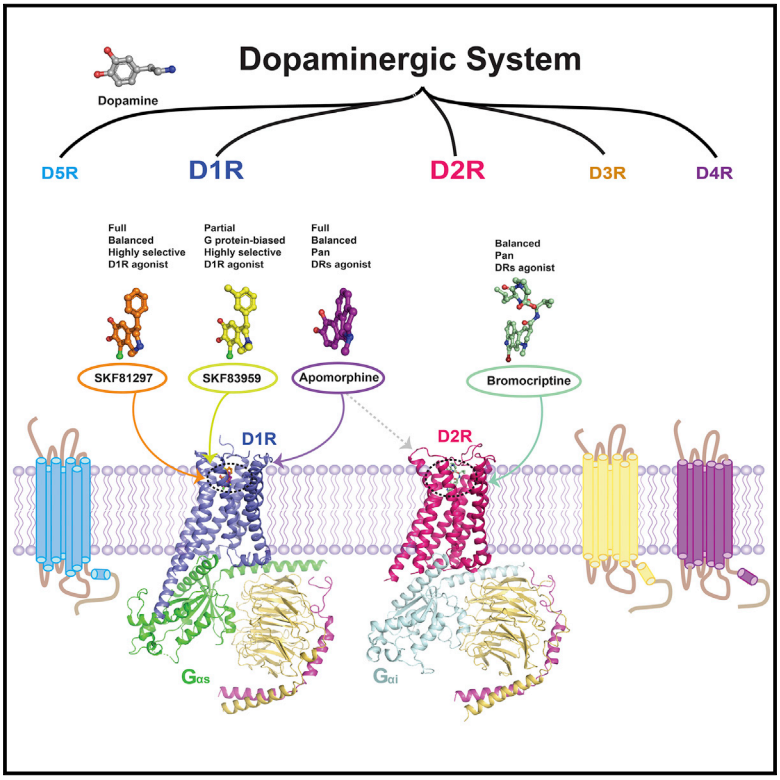

Authors

Youwen Zhuang, Peiyu Xu, Chunyou Mao, ..., Yan Zhang, Cheng Zhang, H. Eric Xu

Correspondence

bryan_roth@med.unc.edu (B.L.R.), chengzh@pitt.edu (C.Z.), eric.xu@simm.ac.cn (H.E.X.), zhang_yan@zju.edu.cn (Y.Z.)

In Brief

Near-atomic resolution structures of activated D1R-G_s and D2R-G_i signaling complexes, together with multiple functional studies, reveal the conserved catechol agonist binding mode in D1R and the structural basis that underlies D1R and D2R ligand selectivity and G protein-coupling specificity.

Highlights

- Structures of dopamine receptor D1R-G_s complexes with three agonists
- Structure of dopamine receptor D2R-G_i complex bound to bromocriptine at 2.8 Å resolution
- Highly similar structures between the active states of D1R and β_2- adrenergic receptor
- Structural determinants for ligand and G protein selectivity between D1R and D2R
- G-protein biased agonism of SKF83959 toward D1R from structural and functional studies

Zhuang et al., 2021, Cell *184*, 931–942
February 18, 2021
https://doi.org/10.1016/j.cell.2021.01.027

CellPress

Cell

CellPress

Article

Structural insights into the human D1 and D2 dopamine receptor signaling complexes

Youwen Zhuang,[1,2,12] Peiyu Xu,[1,2,3,12] Chunyou Mao,[3,4,5,12] Lei Wang,[6,12] Brian Krumm,[7,12] X. Edward Zhou,[8,12] Sijie Huang,[1,2,9] Heng Liu,[6] Xi Cheng,[10] Xi-Ping Huang,[7] Dan-Dan Shen,[3,4,5] Tinghai Xu,[8] Yong-Feng Liu,[7] Yue Wang,[1,2] Jia Guo,[1,2] Yi Jiang,[1,2] Hualiang Jiang,[10] Karsten Melcher,[8] Bryan L. Roth,[7,*] Yan Zhang,[3,4,5,11,*] Cheng Zhang,[6,*] and H. Eric Xu[1,2,9,13,*]

[1]The CAS Key Laboratory of Receptor Research, Shanghai Institute of Materia Medica, Chinese Academy of Sciences, Shanghai 201203, China

[2]University of Chinese Academy of Sciences, Beijing 100049, China

[3]Department of Biophysics and Department of Pathology of Sir Run Run Shaw Hospital, Zhejiang University School of Medicine, Hangzhou 310058, China

[4]Zhejiang Laboratory for Systems and Precison Medicine, Zhejiang University Medical Center, Hangzhou 311121, China

[5]MOE Frontier Science Center for Brain Research and Brain-Machine Integration, Zhejiang University School of Medicine, Hangzhou 310058, China

[6]Department of Pharmacology and Chemical Biology, School of Medicine, University of Pittsburgh, Pittsburgh, PA 15213, USA

[7]Department of Pharmacology, University of North Carolina at Chapel Hill, Chapel Hill, NC 27599-7365, USA

[8]Center for Cancer and Cell Biology, Program for Structural Biology, Van Andel Research Institute, Grand Rapids, MI, USA

[9]School of Life Science and Technology, ShanghaiTech University, Shanghai 201210, China

[10]State Key Laboratory of Drug Research and CAS Key Laboratory of Receptor Research, Shanghai Institute of Materia Medica, Chinese Academy of Sciences, Shanghai 201203, China

[11]Zhejiang Provincial Key Laboratory of Immunity and Inflammatory Diseases, Hangzhou 310058, China

[12]These authors contributed equally

[13]Lead contact

*Correspondence: bryan_roth@med.unc.edu (B.L.R.), zhang_yan@zju.edu.cn (Y.Z.), chengzh@pitt.edu (C.Z.), eric.xu@simm.ac.cn (H.E.X.)

https://doi.org/10.1016/j.cell.2021.01.027

SUMMARY

The D1- and D2-dopamine receptors (D1R and D2R), which signal through G_s and G_i, respectively, represent the principal stimulatory and inhibitory dopamine receptors in the central nervous system. D1R and D2R also represent the main therapeutic targets for Parkinson's disease, schizophrenia, and many other neuropsychiatric disorders, and insight into their signaling is essential for understanding both therapeutic and side effects of dopaminergic drugs. Here, we report four cryoelectron microscopy (cryo-EM) structures of D1R-G_s and D2R-G_i signaling complexes with selective and non-selective dopamine agonists, including two currently used anti-Parkinson's disease drugs, apomorphine and bromocriptine. These structures, together with mutagenesis studies, reveal the conserved binding mode of dopamine agonists, the unique pocket topology underlying ligand selectivity, the conformational changes in receptor activation, and potential structural determinants for G protein-coupling selectivity. These results provide both a molecular understanding of dopamine signaling and multiple structural templates for drug design targeting the dopaminergic system.

INTRODUCTION

Dopamine is a catecholamine neurotransmitter with important functions for both the central (CNS) and peripheral (PNS) nervous systems. Dopaminergic functions are mediated by a family of five G-protein-coupled receptors, which are divided into two groups: the D1-like and the D2-like receptors (Figure 1A). The D1-like group, including D1R and D5R, primarily couple to the stimulatory G protein G_s, whereas the D2-like group, including D2R, D3R, and D4R, primarily couple to the inhibitory G protein $G_{i/o}$. Among the five dopamine receptors, D1R and D2R are the most abundant receptors in the CNS, especially in the basal ganglia and the prefrontal cortex (Beaulieu and Gainetdinov, 2011; Missale et al., 1998). Aberrant D1R and D2R signaling has been associated with many neuropsychiatric diseases including Parkinson's disease (PD), schizophrenia, various types of cognitive impairment, attention-deficit hyperactivity disorder (ADHD), drug abuse, and autism (Abi-Dargham et al., 2002; Beaulieu and Gainetdinov, 2011; Beninger and Miller, 1998; Kostrzewa et al., 2018; Lemon and Manahan-Vaughan, 2006; McNab et al., 2009; Vijayraghavan et al., 2007). Activation of dopaminergic pathways through D1R and D2R has been proposed to mediate various aspects of the reinforcing and rewarding properties of many abused drugs (Di Chiara et al.,

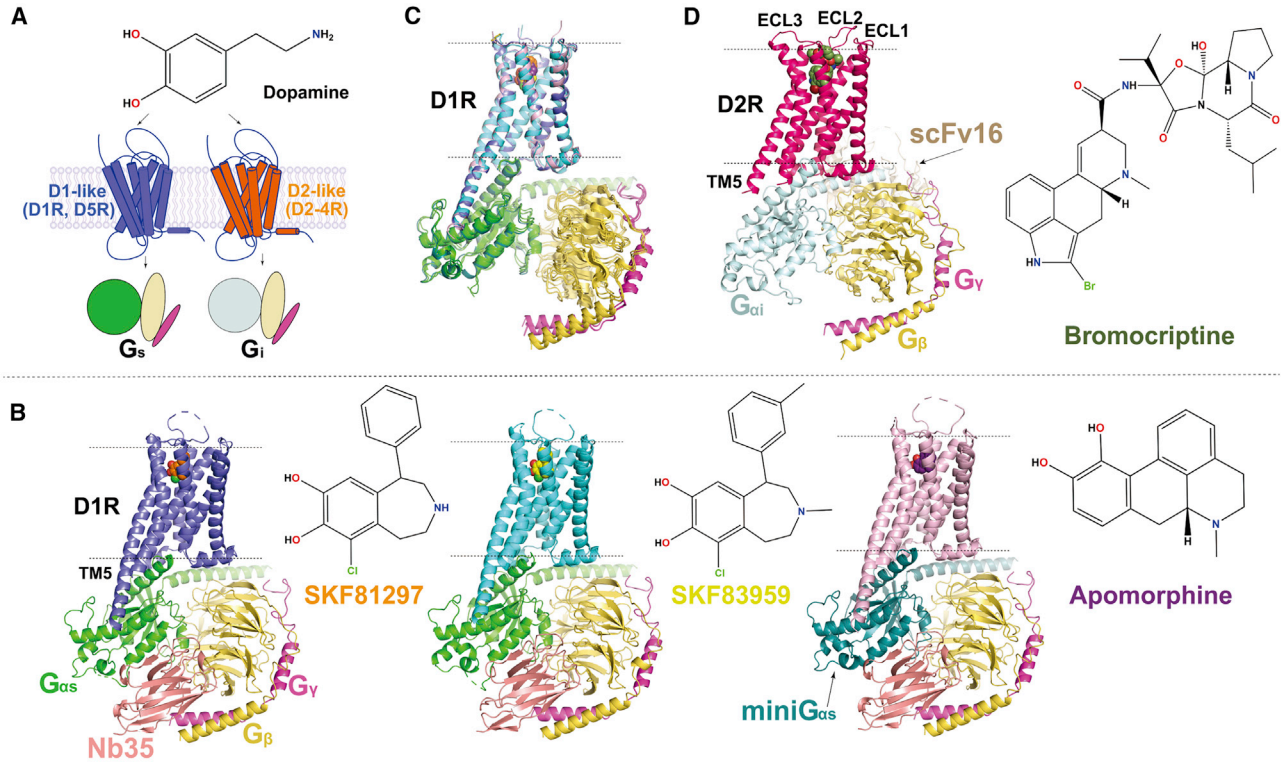

Figure 1. Overall structures of D1R and D2R signaling complexes

(A) Dopamine signaling through D1-like and D2-like dopamine receptors.

(B) Structures of the D1R-G_s with SKF83959 and SKF81297 and the D1R-miniG$_s$ with apomorphine. The receptor is colored slate, cyan, and pink, respectively. See Figure S2 and Table S1.

(C) Alignment of three structures of D1R signaling complexes shown in (B).

(D) Structure of the D2R-G_i with bromocriptine. The D2R is colored hot pink. See Figure S2 and Table S1.

See also Figures S1, S3, and S4.

2004; Volkow and Morales, 2015). Given the centrality of the dopaminergic system, many ligands targeting D1R and D2R have been developed for treating diverse CNS disorders by maintaining normal dopaminergic homeostasis and restoring homeostasis in disease states.

Due to the high homology of dopamine receptors, most dopaminergic drugs are highly polypharmacologic because they frequently target multiple dopamine receptors and other aminergic GPCRs (Butini et al., 2016; Roth et al., 2004). Non-selective dopamine agonists, including PD drugs apomorphine (Di Chiara and Gessa, 1978) and bromocriptine (Parkes et al., 1976), have been proposed to be more effective than selective drugs for treating complex CNS diseases (Roth et al., 2004). On the other hand, highly selective dopamine receptor ligands are important pharmacological tools for functional investigation. The first selective ligands of D1R were phenyl benzazepine derivatives, including the SKF compounds (e.g., SKF81297 and SKF83959) as D1R agonists and the D1R antagonist SCH23390, which have been used for decades to study D1R pharmacology and physiology (Hall et al., 2019; Neumeyer et al., 2003).

To date, no D1R structure has been reported. Several crystal structures of antagonist-bound D2R, D3R, and D4R and a 3.7 Å structure of a thermostabilized D2R-G_i complex bound to bromocriptine have been reported (Chien et al., 2010; Fan et al., 2020; Wang et al., 2017, 2018; Yin et al., 2020). The lack of D1R structures has impeded both our understanding of the molecular basis of D1R signaling and our ability to prosecute structure-guided drug discovery at D1R. In addition, the thermostabilized D2R-G_i complex contains thermostabilizing mutations and truncation of intracellular loop 3 (ICL3) in D2R, making it difficult to rationalize the relevance of ligand binding mode, TM conformations, and G protein coupling characteristics to the wild-type D2R. Here, we report four cryo-electron microscopy (cryo-EM) structures of the human D1R-G_s and D2R-G_i protein complexes: three structures of the wild-type D1R-G_s complexes, either with the pan dopamine agonist drug apomorphine at a global resolution of 3.0 Å, or with D1R/D5R-selective catechol agonists SKF81297 and SKF83959 at a global resolution of 3.0 Å and 2.9 Å, respectively, and one structure of the human wild-type D2R-G_i complex with the D2R/D3R agonist drug bromocriptine at a global resolution of 2.8 Å. These structures reveal the basis for agonist selectivity, G protein selectivity, and receptor activation at D1R and D2R. The structures also provide multiple templates for rational design of dopaminergic ligands aimed for treating CNS diseases.

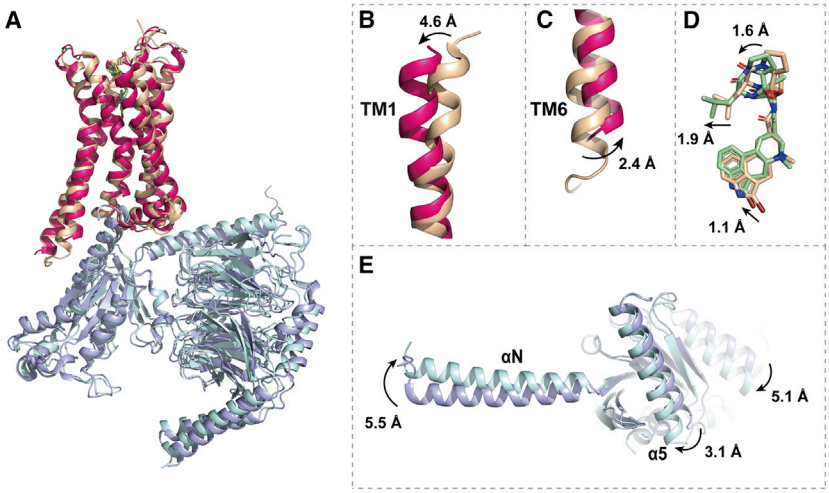

Figure 2. Structure comparison of bromocriptine-D2R-G_i complexes

(A) Alignment of the structure of bromocriptine-D2R-G_i complex reported by us and the structure of thermostabilized D2R complexed with G_i and bromocriptine in nanodiscs reported previously (PDB: 6VMS). The receptor and G_i protein are colored hot pink and pale cyan, respectively, in our structure. The thermostabilized receptor and the ligand bromocriptine are colored light brown, and the G_i protein is colored light blue in the previously reported structure. Bromocriptine is colored light green in our structure. See Figure S5 for amino acid sequence alignment between WT D2R and thermostabilized D2R.

(B–E) Structural differences of the two bromocriptine-D2R-G_i complexes in TM1 (B), TM6 (C), and ligand binding mode (D) of receptor part and $G_{\alpha i}$ of G protein part (E).

RESULTS AND DISCUSSION

Overall structures of agonist-bound D1R-G_s and D2R-G_i complexes

For cryo-EM studies, we fused the wild-type human D1R (referred as WT D1R hereafter) to a prolactin signal peptide, followed by FLAG and 8× His tags for expression and purification (Figure S1). We co-expressed D1R with a dominant negative form of human $G_{\alpha s}$ containing two mutations (G226A and A366S) (Liu et al., 2016), rat $G_{\beta 1}$ and bovine $G_{\gamma 2}$ in Sf9 insect cells, to form the D1R-G_s complexes with SKF81297 and SKF83959. An engineered mini$G_{\alpha s}$ construct based on the previously reported mini$G_{\alpha s}$ sequence (Carpenter et al., 2016) with the same dominant negative mutations was used for obtaining the apomorphine-activated D1R-G_s complex (Figure S1B). A single-chain antibody, Nb35, was added to stabilize the nucleotide-free D1R-G_s complexes (Rasmussen et al., 2011b). To obtain the human D2R-G_i complex bound to bromocriptine, we co-expressed the full-length human D2R long form (Giros et al., 1989; Monsma et al., 1989) fused with an N-terminal BRIL protein (Chun et al., 2012) (Figure S1H) with a dominant negative form of human $G\alpha_{i1}$ containing four mutations (S47N, G203A, E345A, and A326S) (Liang et al., 2018), the rat $G_{\beta 1}$, and bovine $G_{\gamma 2}$ in Sf9 insect cells. The single-chain antibody fragment scFv16 was added to stabilize the nucleotide-free bromocriptine-D2R-G_i complex (Koehl et al., 2018). All complexes were purified to homogeneity for single-particle cryo-EM analysis (Figure S1).

The structures of SKF81297-, SKF83959-, and apomorphine-bound D1R-G_s complexes were determined with global resolutions of 3.0 Å, 2.9 Å, and 3.0 Å, respectively (Figures 1B, S2, S3, and S4; Table S1). The relatively high resolution density maps of the three complexes allowed us to clearly model most portions of D1R from residues S21 to Y348, the entire molecules of SKF81297, SKF83959, apomorphine, the G_s heterotrimer, and Nb35 (Figures 1B, 1C, S3, and S4). In addition, several putative cholesterol molecules and lipid acyl chains were modeled surrounding the D1R transmembrane domain (TMD) (Figures S2A–S2C), the corresponding densities could be either cholesteryl hemisuccinate (CHS) or cholesterol, but were modeled as cholesterol. In all three structures, the N-terminal region preceding TM1 and ICL3 of D1R and the α-helical domain (AHD) of $G_{\alpha s}$ were poorly observed and not modeled due to their flexibilities, which is consistent with most GPCR-G protein complex structures reported to date.

The structure of the D2R-G_i complex bound to bromocriptine in detergent was determined at a global resolution of 2.8 Å with a much improved density map compared to the previously reported 3.7 Å cryo-EM structure of the thermostabilized D2R complexed with G_i heterotrimer in lipid nanodiscs (Figure S4), which provided an unambiguous modeling of most parts of the D2R, the G_i protein, and bromocriptine (Figures S2D and S4). A majority of the side chains of D2R from Y34 to L441 were well defined except for a part of ICL3 (residues K226 to S364) (Figures 1D, S2D, and S4). In particular, the structures of all three extracellular loops 1-3 (ECL1–ECL3) of D2R were clearly defined. Unlike the D1R-G_s structures, there was no clear density of cholesterol and lipid molecules surrounding the transmembrane domain of D2R as was observed in the D2R-G_i structure (Figure S2D).

Although the overall structure of the bromocriptine-bound D2R-G_i complex is similar to the previously reported 3.7 Å structure of a thermostabilized D2R-G_i complex bound to the same ligand reconstituted in the nanodiscs (Yin et al., 2020), with root-mean-square deviation (RMSD) values of 0.9 Å for the Cα atoms of the whole complexes and 0.7 Å for the Cα atoms of D2R alone (Figures 1D and 2A), several significant differences are observed between the two structures. These include a noticeable 2.4 Å shift at the cytoplasmic end of TM6 (Figure 2) and a 6.7° difference in the orientation of α5 helix of $G_{\alpha i}$ relative to the receptor (Figure 2). In addition, the wild-type D2R structure displays a regular helical structure in the N-terminal half of TM1 instead of the 3^{10}-like irregular helix in the thermostabilized D2R structure (Figure 2). Interestingly, there is an ~1–2 Å shift in the

binding mode of bromocriptine in our structure compared to the previous structure, which is accompanied by different conformations of the surrounding residues including $I184^{ECL2}$ and $W386^{6.48}$ that play important roles in D2R activation (Yin et al., 2020) (Figure 2). These differences between the two structures may be attributed to: (1) the stabilizing mutations and the truncation at ICL3 of the thermostabilized D2R used in the previous study (Figure S5), (2) the different resolutions between the two structures, and (3) the different detergent and lipid environment of the D2R-G_i complex used in the current and previous studies.

Conserved and divergent features of agonists recognition at D1R

In all three D1R-G_s complexes, D1R displays a canonical transmembrane domain (TMD) with a ligand binding pocket located at the extracellular side of the TMD and a G-protein binding cavity at the cytoplasmic side (Figure 1B). Apomorphine, SKF81297, and SKF83959 share common catechol motifs, with SKF83959 having two additional methyl groups as compared with SKF81297 (Figure 1B). The overall structures of D1R bound to three agonists are highly similar (Figures 1B and 1C), with RMSD values of 0.2 Å for the Cα atoms of D1R between SKF81297 and apomorphine-bound structures and 0.5 Å for the Cα atoms of D1R between SKF81297 and SKF83959-bound structures.

In the structures, SKF81297 and SKF83959 share nearly the identical binding poses, with a similar "L"-shape configuration, in which the phenyl group is extended toward extracellular loop 2 (ECL2) (Figures 3A, 3B, and 3D). The benzazepine rings of SKF81297 and SKF83959 are located at the bottom of the orthosteric pocket, with the catechol group facing TM5 (Figure 3D). The benzazepine rings are sandwiched by TM3 on one side and by TM6/7 on the other, leading the amine group to form a close ionic interaction with the carboxylate group of $D103^{3.32}$ (superscript based on Ballesteros-Weinstein numbering rules of GPCRs (Ballesteros and Weinstein, 1995)) from TM3, which is highly conserved among aminergic GPCRs (Vass et al., 2019) (Figures 3A and 3B). In both structures, the *meta*-hydroxyl from the catechol group forms hydrogen bonds with $S198^{5.43}$, whereas the *para*-hydroxyl makes a hydrogen bond with $N292^{6.55}$. In the SKF83959-bound D1R structure, the ligand is pushed closer toward TM5 due to an additional methyl group in the azepine ring, which is packed against $W321^{7.43}$ (Figure 3D). The *para*-hydroxyl group from SKF83959 makes another hydrogen bond with $S198^{5.43}$, whereas the *meta*-hydroxyl group forms a direct hydrogen bond with $S202^{5.46}$, which is absent in the SKF81297-bound D1R structure (Figure 3D). The extensive network of polar interactions by SKF81297 and SKF83959 may explain their high affinities for D1R. Besides the polar interaction network, the three ring structures of SKF81297 and SKF83959 also engage in extensive hydrophobic interactions with nearby residues from TM3, TM6-7, and ECL2 (Figures 3A and 3B).

Compared to SKF81297 and SKF83959, apomorphine occupies nearly an identical binding pocket (Figures 3C, 3E, and 3F). The four-ring scaffold of apomorphine nearly overlaps with the three-ring structure of SKF compounds, with the two hydroxyl groups form the catechol moiety and the amine group are located in essentially the same positions, thus engaging in a similar set of interactions with D1R (Figure 3C). A significant distinction between apomorphine and the SKF compounds is that the benzyl rings of SKF81297 and SKF83959 (Figures 3E and 3F) protrude further upward to ECL2.

To correlate the structural observations with the ligand binding activity, we individually mutated most of the ligand pocket residues and assessed their effects on expression levels, their ability to bind ligands using radioligand competition binding assays, and their ability to stimulate cyclic AMP (cAMP) production and β-arrestin recruitment assays. We used a tritiated D1R antagonist, [^{3}H]SCH23390, which shares high chemical similarity with the SKF compounds. Consistent with other aminergic GPCRs (Vass et al., 2019), mutation of the conserved $D103^{3.32}$A, which forms hydrogen bonds with the conserved amine group in all ligands, resulted in the loss of all binding of [^{3}H]SCH23390 in saturation binding experiments and loss of cAMP production in the Glosensor assay (Figures 3A–3C; Table S2). Additionally, mutations of residues in the orthosteric binding pocket (OBP) that directly interact with SKF81297, SKF83959, and apomorphine, $I104^{3.33}$A, $L190^{ECL2}$A, $S198^{5.42}$A, $S199^{5.43}$A, $N292^{6.55}$A/H, and $W321^{7.43}$Y, all displayed decreased binding of [^{3}H]SCH23390 when compared to WT D1R, suggesting that SCH23390 might adopt a similar binding pose as to those three agonists (Figures 3A–3C; Table S2). Results from the [^{3}H]-SCH23390 competing binding analysis and cAMP production assays further support the binding modes of SKF81297, SKF83959, and apomorphine. Mutations of residues $D103^{3.32}$ and $S198^{5.42}$, which are highly conserved in aminergic receptors and play critical roles in receptor activation(Vass et al., 2019), led to either a loss of or compromised activity of each agonist (Figure 3G; Tables S3 and S4). In addition, mutations of other residues around the pocket, including $K81^{2.61}$, $I104^{3.33}$, $S107^{3.36}$, $L190^{ECL2}$, $S199^{5.43}$, and $N292^{6.55}$, also reduced activities of the three agonists (Figure 3G; Tables S3 and S4). For each agonist, its *para*-hydroxyl group interacts weakly with $S199^{5.43}$ but forms strong hydrogen bonds with $S198^{5.42}$ and its *meta*-hydroxyl group forms hydrogen bonds with $N292^{6.55}$. In cAMP assays, the $S199^{5.43}$A mutation displayed a similar pEC_{50}, whereas mutations $S198^{5.42}$A and $N292^{6.55}$A displayed significantly greater reduction in pEC_{50} for each compound when compared to the WT D1R (Figure 3G; Table S4), supporting the binding modes of SKF81297, SKF83959, and apomorphine in their respective structures.

Several mutations displayed different effects for SKF81297, SKF83959, and apomorphine in the cAMP production assays, which may be caused by the slightly different binding modes of these agonists. The mutation $S202^{5.46}$A resulted in greater reduction in pEC_{50}s for SKF83959 and apomorphine than for SKF81297(Figures 3G and S6; Table S4), consistent with their differences in forming hydrogen bonds with $S202^{5.46}$ (Figures 3D–3F). The greater reduction in pEC_{50} values for the two SKF compounds than for apomorphine caused by the mutation $L190^{ECL2}$A is likely due to the closer distance between the SKF compounds and ECL2 (Figures 3E–3G and S6; Table S4). The mutation $N292^{6.55}$H led to an increased pEC_{50} for apomorphine but significantly decreased pEC_{50}s for the SKF compounds (Figures 3G and S6; Table S4), which may be due to a potential steric clash between the histamine residue and the benzyl ring of the SKF compounds.

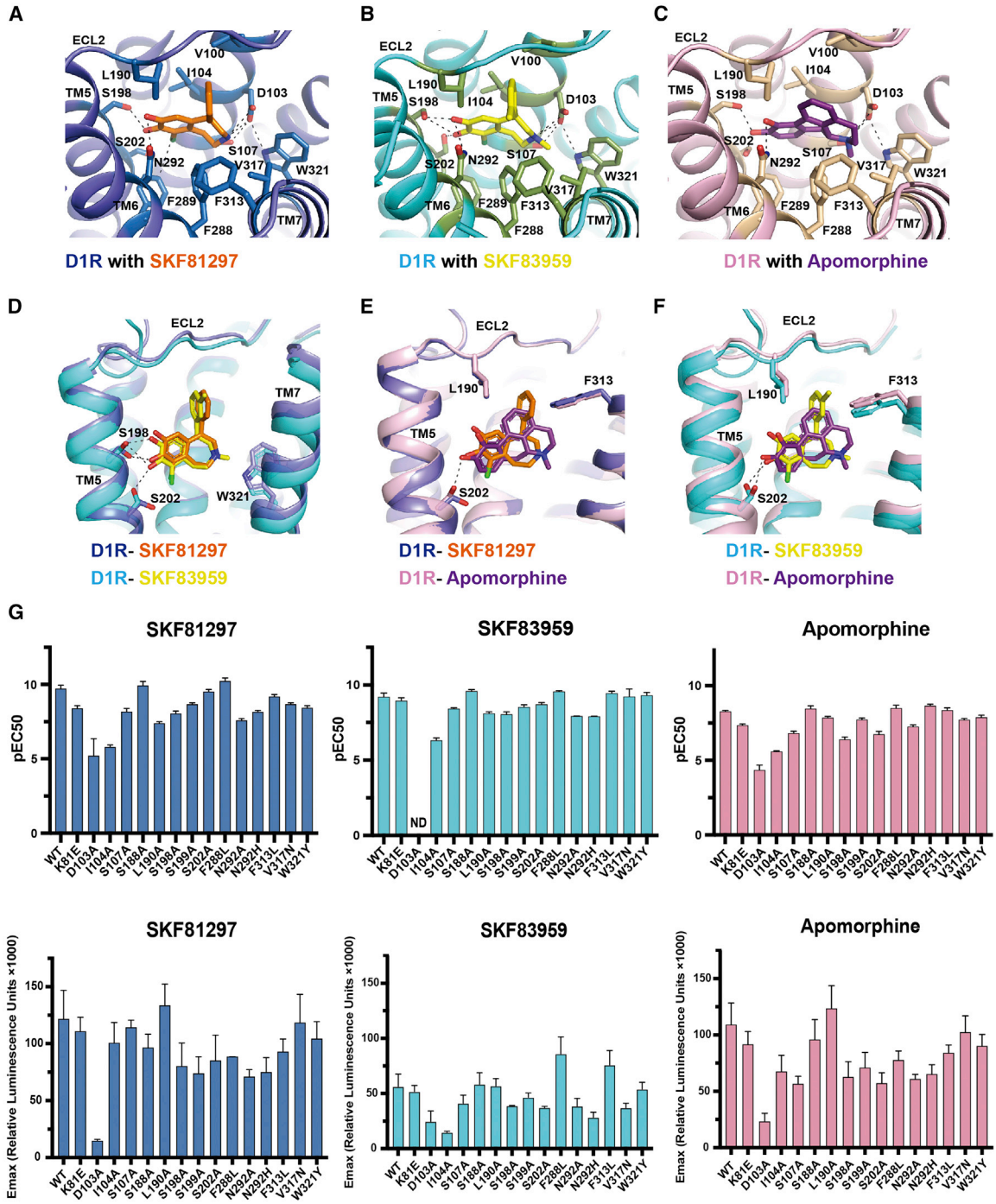

Figure 3. Agonists recognition at D1R

(A–C) Interactions between SKF81297 (orange), SKF83959 (yellow), and apomorphine (purple) with D1R. The receptor is colored slate, cyan, and pink, respectively.

(D–F) Comparisons of binding poses between SKF81297 and SKF83959 (D), SKF81297 and apomorphine (E), and SKF83959 and apomorphine (F) when aligned in D1R receptor part. Hydrogen bonds are shown as black dash lines.

(G) G_s-cAMP accumulation results of WT D1R and D1R mutants activated by SKF81297, SKF83959, and apomorphine, respectively. Activities of the three agonists are identified as pEC_{50}. ND, not detected. Average Emax values were determined from "log(agonist) versus response-variable slope (four parameters)" function in GraphPad Prism 8.4 software (GraphPad Software Inc., San Diego, CA) and were divided by 10^3 for display. All data are presented as mean values ± SEM with a minimum of four technical replicates and n = 3 biological replicates. See Figure S6 for dose response curves and Table S4 for fitted parameter values. See also Tables S2 and S3.

Although the D1R belongs to the same dopamine receptor family as D2-like receptors, the closest phylogenetic neighbors of D1R are the β-adrenergic receptors (βARs) that also couple to G_s (Vass et al., 2019). It was suggested previously that the endogenous catecholamine βAR agonist epinephrine (EP) can also activate dopamine receptors but with much less potency (Lanau et al., 1997; Sánchez-Soto et al., 2016). The structure of the β_2AR in complex with EP has been reported (Ring et al., 2013). Alignment of the structures of D1R-SKF81297 and β_2AR-EP revealed similar receptor interaction patterns for these two ligands with a main difference in the interaction with residues of TM7. In the structure of β_2AR-EP, N312$^{7.39}$ and Y316$^{7.43}$ form direct hydrogen bond interactions with EP. Instead, in the structure of D1R-SKF81297, the corresponding residues V317$^{7.39}$ and W321$^{7.43}$ adopt no direct polar interactions but hydrophobic interaction with SKF81297 (Figure S7A). We further analyzed the binding affinities of the two catecholamine β_2AR agonists EP and isoproterenol (ISO), to the wild-type D1R, the D1R mutants V317N, W321Y individually, and the D1R mutant containing both V317N and W321Y. We found that the WT D1R could be activated by EP and ISO to similar extents. Both V317N and V317N/W321Y D1R mutants showed increased binding affinities to ISO and EP, whereas the W321Y mutation had no effect on the binding affinities of these two compounds to D1R, demonstrating that the D1R residue V317$^{7.39}$ is important for the selectivity of D1R for dopamine over other catecholamines, including EP (Figure S7B; Table S5).

Partial and biased agonism of SKF83959

Although SKF83959 and SKF81297 share highly similar chemical structures, their potency in inducing G_s signaling differs significantly, which is likely due to the slightly different binding poses of SKF81297 and SKF83959 (Figures 3D, 3G, and S6) (Lee et al., 2014). Compared to SKF81297, SKF83959 is closer to TM5 due to the steric effects between the extra methyl groups in SKF83959 and D1R residues F313$^{7.35}$ and W321$^{7.43}$ (Figures 3B and 3D). Previous structural studies on the β_2AR suggested that agonists can induce an inward movement of TM5 in the ligand-binding pocket, which is associated with the conformational changes at the cytoplasmic region during receptor activation (Rasmussen et al., 2011a). In addition, the β_2AR partial agonist salmeterol has been suggested to have a weaker effect on stabilizing the inward movement of TM5 compared to the β_2AR full agonist epinephrine, resulting in its lower efficacy (Masureel et al., 2018). Similarly, in the D1R structures, the closer distance between SKF83959 and TM5 as a result of steric effects between methyl groups of SKF83959 and D1R residues F313$^{7.35}$ and W321$^{7.43}$ may lead to a weaker ability of SKF83959 in inducing the inward movement of TM5 and thus a lower efficacy of SKF83959 compared to SKF81297. Supporting this hypothesis, it has been shown that removing one methyl group in SKF83959 could increase its efficacy (Lee et al., 2014). In addition, mutations of F313$^{7.35}$ and W321$^{7.43}$ to residues with smaller side chains, which potentially eliminated their steric restrictions on SKF83959, led to comparable efficacy of SKF83959 and SKF81297 in our cAMP accumulation assays (Figure S6).

Interestingly, previous studies also showed that although both SKF compounds could activate the G_s-cAMP signaling pathway, only SKF81297, but not SKF83959, could stimulate β-arrestin recruitment (Conroy et al., 2015). This is consistent with the result from our β-arrestin recruitment assays (Table S6). The subtle differences in the binding modes of the two SKF compounds revealed by our structures and mutagenesis studies may lead to distinct assembly of conformational states of D1R associated with different signaling properties. To illustrate the structural determinants of β-arrestin biased activity of SKF83959, we individually detected the β-arrestin recruitment activities of D1R mutants with mutations of residues near the binding pocket induced by dopamine, SKF81297, and SKF83959 through Tango assay (Table S6). The results showed that F288L could significantly increase the maximum β-arrestin recruitment for both SKF83939 and SKF81297, whereas F288A could cause the opposite effect by reducing β-arrestin recruitment for both ligands. F289A could also lead to increased β-arrestin recruitment for both ligands but to a much less extent than that induced by F288L. Interestingly, the mutation V317A could almost abolish SKF81297-induced β-arrestin recruitment but slightly increase that induced by SKF83959 (Table S6). All of these results suggested important roles of F288$^{6.51}$, F289$^{6.52}$, and V317$^{7.39}$ in the D1R agonist-induced β-arrestin recruitment. In our structure, the V317$^{7.39}$, F288$^{6.51}$, and W321$^{7.43}$ residues participate in the hydrophobic packing with the methyl group in the azepine ring of SKF83959 compound (Figure 3B), suggesting that such methyl group is vital in the biased activity of SKF83959 to D1R. Moreover, previous studies reported that other SKF compounds with bulky side chains attached to the amine group of azepine ring also showed biased signaling activities on D1R similar to SKF83959 (Conroy et al., 2015), further proving the important role of the additional methyl group in SKF83959 for its biased activity.

Activation mechanisms of D1R and D2R

Currently, no structure of the inactive D1R is available to allow proper structural comparison with the active D1R. Nevertheless, we observed that the structures of D1R-G_s signaling complexes are highly similar to the structure of the β_2AR-G_s signaling complex (Figures 4A and 4B). In particular, critical structural elements in β_2AR including three TMs, TM5, TM6, and TM7, the DR$^{3.50}$Y motif, and the core P$^{5.50}$I$^{3.40}$F$^{6.44}$ motif, which undergoes large conformational changes during the activation of β_2AR (Rasmussen et al., 2011b; Steyaert and Kobilka, 2011), can be well aligned to those in D1R (Figures 4C–4E), suggesting a highly conserved activation mechanism for D1R and β_2AR. It is to be noted that the relative orientations of G_s to D1R and to β_2AR in the G_s-coupled structures are highly similar. This is in contrast to the highly diverse modes of coupling of G_i to different GPCRs (Zhuang et al., 2020). One significant structural difference between the D1R-G_s and β_2AR-G_s complexes is that the cytoplasmic end of TM5 of D1R is extended by two additional helical turns compared to that of β_2AR, which forms additional interactions with the Ras-like domain of $G_{\alpha s}$ (Figures 4A and 4B).

For D2R, structural comparison of the active bromocriptine-bound D2R to the inactive risperidone-bound D2R (Wang et al., 2018) indicated large conformational changes at both cytoplasmic and extracellular regions (Figures 5A and 5B). In the inactive D2R structure, the pyrimidine group of risperidone

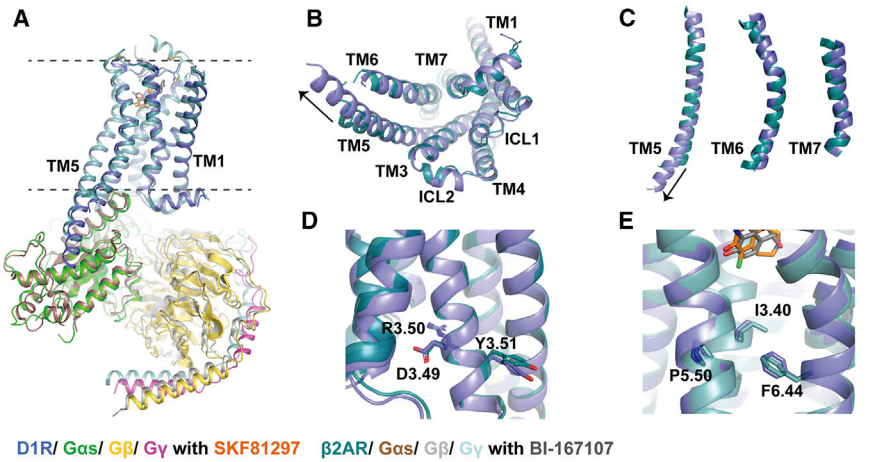

Figure 4. D1R activation

(A) Structural alignment of D1R-G_s bound to SKF81297 and β_2AR-G_s bound to BI-167107 (PDB: 3SN6). The alignment was based on the structures of D1R and β_2AR, which are colored slate and teal, respectively.

(B) Structural comparison of the cytoplasmic regions of D1R and β_2AR.

(C) Alignment of TM5, TM6, and TM7 of D1R and β_2AR.

(D and E) Alignment of the $D^{3.49}R^{3.50}Y^{3.51}$ motifs (D) and the $P^{5.50}I^{3.40}F^{6.44}$ motifs (E) of D1R and β_2AR. See also Figures S2 and S7 and Table S5.

is deeply inserted into the bottom of the ligand binding pocket and forms direct hydrophobic interaction with the toggle switch residue $W386^{6.48}$, thus restricting the downward swing of $W386^{6.48}$ and locking the receptor in its inactive state (Figure 5C). In the active bromocriptine-bound D2R structure, the hydrophobic interactions between bromocriptine and $W386^{6.48}$ result in a downward movement of the toggle switch residue $W386^{6.48}$ (Figure 5C). The swing of $W386^{6.48}$ is accompanied by conformational changes of residue $F403^{6.44}$ in the PIF motif (Figure 5D), $R132^{3.50}$ in the DRY motif (Figure 5E), and an inward movement of TM7 (Figure 5F). These conformational changes are further associated with the breakage of the conserved ionic lock between $R132^{3.50}$ and $E389^{6.30}$ and an outward movement of 9 Å at the cytoplasmic end of TM6 (Figure 5B). Together, these conformational changes open up the TMD cavity to allow the α5 helix of $G_{\alpha i}$ to insert into the TMD of D2R. This activation mechanism is consistent with other class A GPCRs, such as rhodopsin (Kang et al., 2018), A_{2A}R (García-Nafría et al., 2018), and CB2 (Xing et al., 2020).

Ligand selectivity in dopamine receptors D1R and D2R

Although D1R and D2R share a large number of common agonists (Wang et al., 2017), structural comparison of D1R and D2R reveals that their ligand pockets have very distinct topology at the extracellular vestibule (Figures 6A and 6B). The SKF compounds are highly selective D1R agonists, while apomorphine is generally considered as a non-selective dopamine receptor agonist (Andersen and Jansen, 1990; Reichmann et al., 2006). Our structures indicate that the binding poses of SKF81297 and SKF83959 are closer to the ECL2 than that of apomorphine in D1R (Figure 6C). If SKF81297, SKF83959, and apomorphine bound to D2R with similar poses as in D1R, both SKF compounds, but not apomorphine, would clash with ECL2, especially the residue $I184^{ECL2}$ of D2R (Figure 6C), thus accounting in part for its non-selective agonist activity to dopamine receptors. In D1R, the residue $S188^{ECL2}$ at the corresponding position of $I184^{ECL2}$ in D2R has a smaller side chain, which is also moved away from the ligand-binding pocket, resulting in extra space to accommodate the bulky phenyl moieties of SKF81297 and SKF83959 that extend from their core benzazepine ring scaffolds (Figures 6A–6C).

Structural comparison of D1R and D2R also provides insight into the ~50-fold selectivity of bromocriptine for D2R over D1R (De Keyser et al., 1995). Superposition of the D1R and D2R structures reveals that the bromocriptine ergoline ring overlaps with the benzazepine rings of the SKF compounds in the orthosteric binding pocket (OBP) (Figure 6D). The tricyclic peptide group of bromocriptine extends upward to the extended binding pocket (EBP) that is in part formed by ECL2 (Figures 6D). Unlike SKF81297 and SKF83959, bromocriptine adopts a binding pose away from both ECL2 regions of D1R and D2R, thus avoiding the steric clash caused by ECL2 (Figures 6A–6D). The ECL2 sequence of D2R is similar to that of D3R but is greatly divergent from other dopamine receptors (Figure S5B). Compared to D2R, the EBP in D1R is less accessible than that of D2R due to a non-conserved residue $K81^{2.61}$ for the tricyclic peptide group of bromocriptine (Figure 6E). In addition, the extracellular end of TM6 of D1R is shifted 5.5 Å toward the ligand binding pocket, which would clash with the leucine side chain of bromocriptine (Figures 6A and 6F). These structural features explain the selectivity of bromocriptine for D2/3R over D1R. Furthermore, a more restricted binding space in D1R may explain its low ligandability and chemical tractability for drug development (Hall et al., 2019).

Specificity for G protein subtypes between D1R and D2R

D1R and D2R are the prototypical G_s and G_i coupled dopamine receptors and comparisons of the D1R and D2R structures provide the basis for the G protein coupling specificity. Three notable differences are observed at the cytoplasmic side between the active D1R and D2R structures. First, relative to D2R, TM6 of D1R is moved further outward by as much as 8.4 Å as measured at the Cα atoms of D1R $F264^{6.27}$ and D2R $Q365^{6.27}$, the last residue of TM6 (Figure 7A). Second, TM5 of D1R is extended by an additional two and a half helical turns toward the intracellular side to make direct interaction with the $G_{\alpha s}$ Ras domain (Figures 7A–7C). Third, the ICL2 helix of D1R is one helical turn longer than that of D2R and makes more extensive interactions with the hydrophobic pocket formed by the αN helix and α5 C-terminal helix of $G_{\alpha s}$ (Figures 7A and 7D). The interface of D1R-G_s is ~1,520 $Å^2$ in all three D1R-G_s complexes, which is larger than the D2R-G_i interface of 1,088 $Å^2$ (Figure 7B).

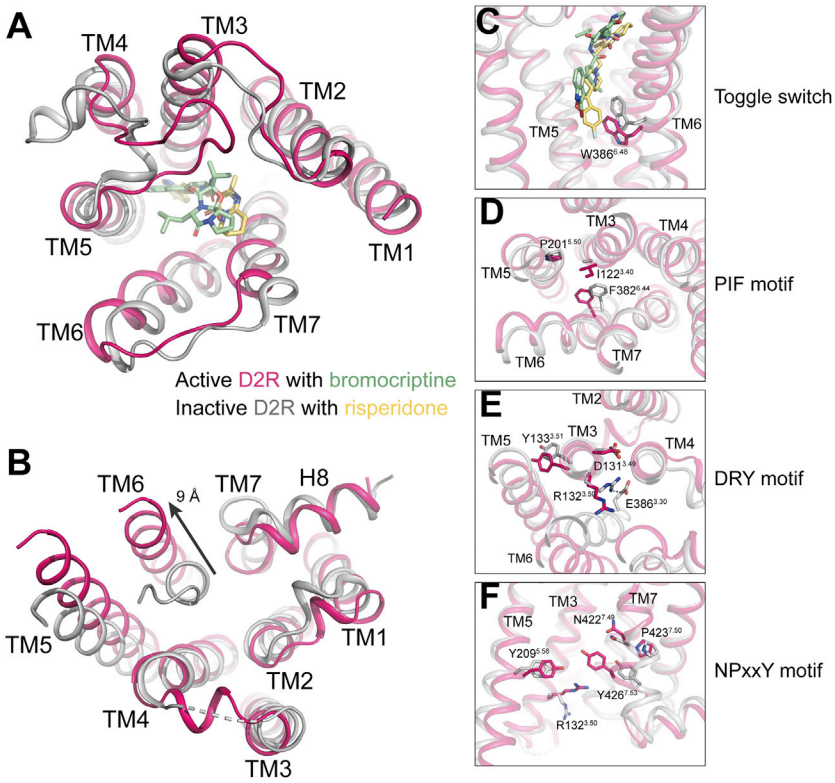

Figure 5. D2R activation

(A and B) Structural comparison of the extracellular regions (A) and the cytoplasmic regions (B) of the active D2R (hot pink) with bromocriptine (light green) and the inactive D2R (light gray) with risperidone (light yellow) (PDB: 6CM4).

(C–F) Different conformations of residues and motifs in the active D2R and the inactive D2R that are involved in receptor activation.

See also Figures S2 and S4.

The differences between the D1R and D2R structures lead to the different coupling mode of G_s and G_i to their corresponding receptors. To accommodate the 8.4 Å outward movement of TM6, the α5 helix of $G_{\alpha s}$ has a 13° clockwise rotation relative to the α5 helix of $G_{\alpha i}$, which leads to an outward shift of 4.8 Å as measured at the Cα atoms of Y391 of $G_{\alpha s}$ and C351 of $G_{\alpha i}$, the last residue from the α5 helix (Figure 7E). Correspondingly, the $G_{\alpha\beta\gamma}$ heterotrimer is rotated by ~20° as measured by the αN helix between the two structures (Figure 7F). Displacement of G_i with G_s in the G protein binding pocket of activated D2R would lead to a severe steric clash between the TM6 and α5 helix of $G_{\alpha s}$. In addition, the relatively narrow G protein binding cavity in the D2R intracellular region is insufficient for adopting the bulkier side chains of the $G_{\alpha s}$ α5 helix. These structural findings imply that the conformations of TM6 and α5 helix play important roles in G_s/G_i selectivity of D1R and D2R, which is consistent with the previous simulation studies of TM6 among rhodopsin, μOR, A_{2a}R, and β_2AR (Kang et al., 2018). In addition, interactions between the extended TM5 and G protein may contribute to additional selectivity for G_s and G_i by D1R and D2R (Figures 7B and 7C).

In conclusion, D1R and D2R are the two prototypical receptors of dopamine signaling and serve as important drug targets for diverse CNS diseases. In this paper, we report four relatively high resolution cryo-EM structures of D1R and D2R signaling complexes bound to the two D1R-selective compounds SKF83959 and SKF81297 and the widely used anti-PD drugs apomorphine and bromocriptine. The structures, together with mutagenesis studies, reveal distinct features of the D1R and D2R ligand binding pockets that determine the D1R-selectivity for the SKF compounds, pan agonism of apomorphine, and the D2R/D3R-selectivity for bromocriptine, the potential activation mechanism for both D1R and D2R, and critical molecular determinants including TM7 residues F313$^{7.35}$, V317$^{7.39}$, and W321$^{7.43}$ of D1R and the extra methyl groups of SKF83959 in comparison to SKF81297 that lead to the partial and biased agonism of SKF83959 on D1R. The structures also reveal the differences in D1R and D2R that serve as the basis for G protein-coupling specificity. Particularly, the outward movement of TM6 and the extension of TM5 in the cytoplasmic side of D1R relative to D2R allow D1R to primarily couple with G_s but not G_i, and for D2R to couple G_i but not G_s. Together, our results provide unprecedented structural insights into the pharmacology and signaling of D1R and D2R and multiple structural templates for rational drug design targeting the dopaminergic system. A companion to this article, "Ligand recognition and allosteric regulationof DRD1-Gs signaling complexes," (Xiao et al., 2021) also appears in this issue of *Cell*.

STAR★METHODS

Detailed methods are provided in the online version of this paper and include the following:

- KEY RESOURCES TABLE
- RESOURCE AVAILABILITY
  - Lead contact
  - Materials availability
  - Data and software availability
- EXPERIMENTAL MODEL AND SUBJECT DETAILS
- METHOD DETAILS
  - Constructs
  - Expression, complex formation and purification
  - Cryo-EM grid preparation and data collection
  - Image processing and map reconstruction
  - Structure model building and refinement
  - Radioligand binding assays
  - Surface expression analysis
  - D1R G_S-mediated G_S-cAMP accumulation assay

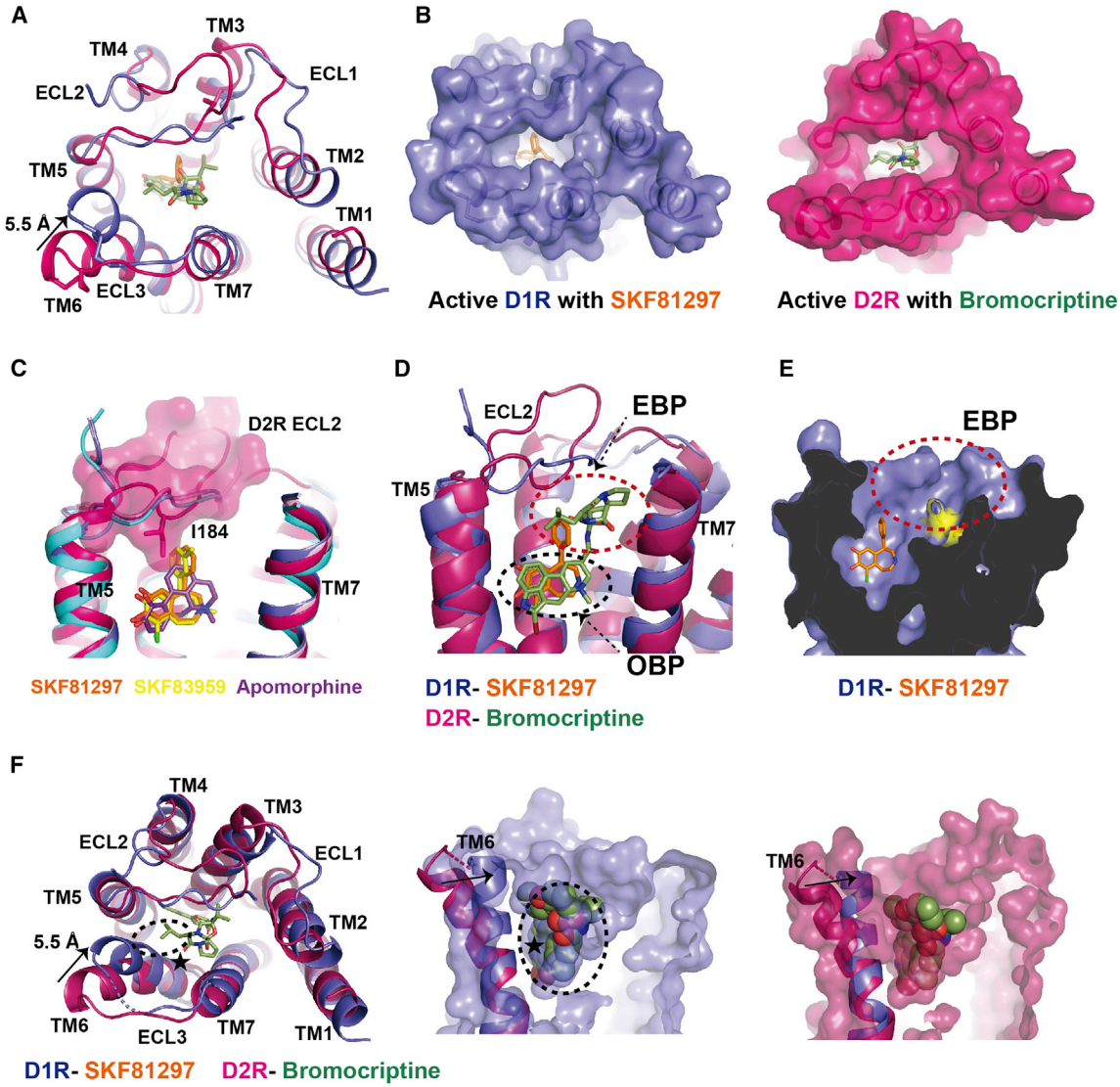

Figure 6. Differences of D1R and D2R in ligand-binding

(A) Structural comparison of the extracellular regions of D1R (slate) and D2R (hot pink). D1R and D2R agonists SKF81297 and bromocriptine are colored orange and light green, respectively.

(B) Agonist-binding pockets of D1R and D2R viewed from the extracellular side.

(C) Structural alignment of the agonist-binding pockets of D1R and D2R. The surface of ECL2 of D2R is shown in hot pink.

(D) Binding poses of the D1R agonist SKF81297 and the D2R agonist bromocriptine. The orthosteric binding pocket (OBP) and the extended binding pocket (EBP) in the D2R for bromocriptine are circled.

(E) Potential EBP in D1R. The residue K81 is shown in yellow.

(F) Extracellular regions. Extracellular ends of TM1, TM6, and TM2 as well as ECL1 in D1R adopt different conformations compared to those in D2R. The narrow D1R ligand binding pocket resulted from the large inward movement of TM6 relative to D2R cause steric clash with bromocriptine. The steric clash regions are circled by dash line and marked with black star. Slate, D1R; hot pink, D2R; light green, bromocriptine.

See also Figures S2, S3, S4, and S5B.

SUPPLEMENTAL INFORMATION

Supplemental Information can be found online at https://doi.org/10.1016/j.cell.2021.01.027.

ACKNOWLEDGMENTS

The cryo-EM data were collected at the Center of Cryo-Electron Microscopy, Zhejiang University, and at the Center of Cryo-Electron Microscopy, Shanghai Institute of Materia Medica. This work was partially supported by the National Key R&D Programs of China (2018YFA0507002 to H.E.X., 2019YFA0508800 to Y. Zhang), Shanghai Municipal Science and Technology Major Projects (2019SHZDZX02 to H.E.X.), CAS Strategic Priority Research Program

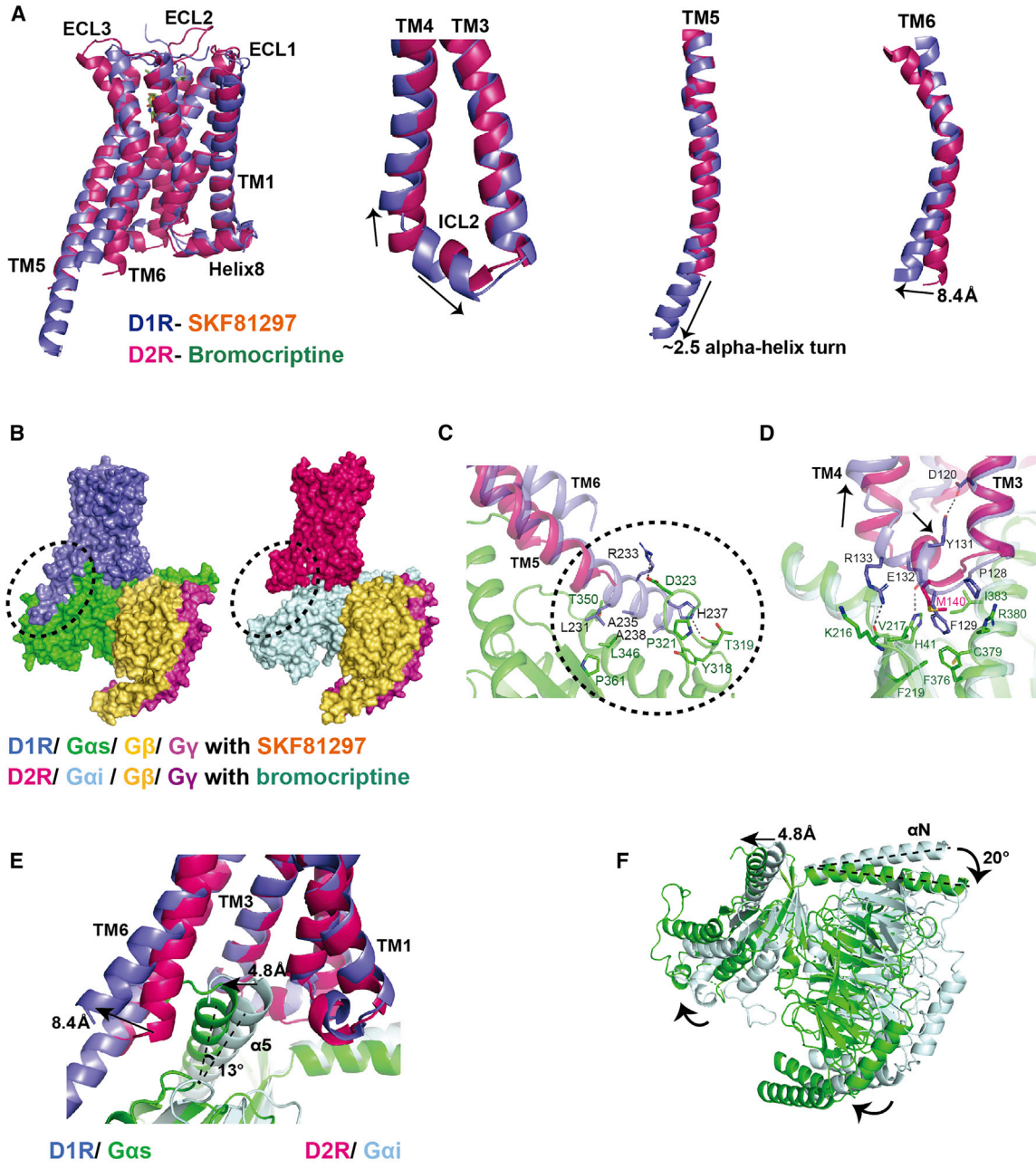

Figure 7. Differences of D1R and D2R G protein-coupling

(A) Structural comparison of the active D1R and D2R showing differences in TM3-ICL2-TM4, TM5, and TM6.

(B) Surface maps of D1R-G_s and D2R-G_i. The extended binding region between D1R and TM5 is circled by dash line, such interaction is absent in D2R-G_i complex. Slate, SKF81297-D1R; hot pink, bromocriptine-D2R; green, $G_{\alpha s}$; pale cyan, $G_{\alpha i1}$; yellow orange, G_{β}; light magentas, G_{γ}.

(C) Interaction between D1R TM5 cytoplasmic end and G_s. The long extended TM5 cytoplasmic end of D1R adopts another binding interface with the Ras-like domain of G_s. Slate, D1R; hot pink, D2R; green, G_s; pale cyan, G_i.

(D) Interaction interface of D1R with ICL2 region of $G_{\alpha s}$. The corresponding region in D2R-G_i complex was aligned. The conformational changes of ICL2 region in D1R relative to D2R were marked with black arrows, compared to D2R, the one more helix turn extending of D1R ICL2 toward G_s hydrophobic pocket leads to stronger hydrophobic interaction between ICL2 and G protein, which is mainly mediated by F129 in ICL2 of D1R. Slate, SKF81297-D1R; green, $G_{\alpha s}$; hot pink, bromocriptine-D2R; pale cyan, $G_{\alpha i}$. The hydrogen bonds are shown in black dash line.

(E) Structural comparison of the binding activities in D1R (slate) and D2R (hot pink) for the α5 helix of $G_{\alpha s}$ (green) and $G_{\alpha i}$ (pale cyan), respectively.

(F) Different orientations of G_s (green) relative to D1R and G_i (pale cyan) relative to D2R. This is based on the alignment of the receptors.

See also Figures S2, S3, and S4.

(XDB37030103 to H.E.X.), the National Natural Science Foundation of China (81922071 to Y. Zhang), Zhejiang Province Natural Science Fund for Excellent Young Scholars (LR19H310001 to Y. Zhang), the Fundamental Research Funds for the Central Universities (2019XZZX001-01-06 to Y. Zhang), the Science and Technology Commission of Shanghai Municipality (20431900100 to H.J.), the Jack Ma Foundation (2020-CMKYGG-05 to H.J.), the National Natural Science Foundation of China (31770796 to Y.J.), the National Science and Technology Major Projects (2018ZX09711002-002-002 to Y.J.), NIMH (Psychoactive Drug Screening Program to X.-P.H., L.Y., and B.L.R. and RO1MH112205 to B.K. and B.L.R.), and NIH (R35GM128641 to C.Z.).

AUTHOR CONTRIBUTIONS

Y. Zhuang designed the expression constructs, prepared protein samples for D1R-G_s complexes for cryo-EM data collection, performed cryo-EM grids preparation, data acquisition, and structure determination of D1R-SKF83959-G_s, and prepared the draft of the manuscript and figures. P.X. and S.H. designed the constructs, prepared the protein sample, conducted cryo-EM data collection and structure determination of D2R-bromocriptine-G_i, and prepared the figures. C.M. and D.-D.S. evaluated the specimen via negative-stain EM, screened the cryo-EM conditions, prepared the cryo-EM grids, collected cryo-EM images, performed cryo-EM map calculation of the SKF81297 and apomorphine-bound D1R-G_s complexes, and participated in the preparation of supplementary figures. B.K., X.-P.H., and Y.-F.L. performed radioligand binding, cAMP assays and β-arrestin recruitment Tango assays. X. Zhang built the models and refined the structures. L.W., H.L., and T.X. performed the first experiments to obtain D1R-G_s and D2R-G_i complexes for cryo-EM data collection at Van Andel Institute and the initial mutagenesis studies on D1R. X.C. and H.J. performed ligand docking and simulation. Y.W. and J.G. helped D1R sample preparation. Y.J. participated in the supervision of the project. K.M. supervised X.E.Z. and participated in manuscript editing. B.L.R. supervised pharmacological and mutagenesis experiments and participated in manuscript writing. C.Z. conceived the project, supervised L.W. and H.L., and prepared the manuscript and figures. Y. Zhang supervised P.X., C.M., D.-D.S., and the EM works. H.E.X. conceived and supervised the project and wrote the manuscript with B.L.R., Y. Zhuang, and C.Z.

DECLARATION OF INTERESTS

The authors declare no competing interests.

Received: August 14, 2020
Revised: December 2, 2020
Accepted: January 15, 2021
Published: February 10, 2021

REFERENCES

Abi-Dargham, A., Mawlawi, O., Lombardo, I., Gil, R., Martinez, D., Huang, Y., Hwang, D.R., Keilp, J., Kochan, L., Van Heertum, R., et al. (2002). Prefrontal dopamine D1 receptors and working memory in schizophrenia. J. Neurosci. *22*, 3708–3719.

Adams, P.D., Afonine, P.V., Bunkóczi, G., Chen, V.B., Davis, I.W., Echols, N., Headd, J.J., Hung, L.W., Kapral, G.J., Grosse-Kunstleve, R.W., et al. (2010). PHENIX: a comprehensive Python-based system for macromolecular structure solution. Acta Crystallogr. D Biol. Crystallogr. *66*, 213–221.

Andersen, P.H., and Jansen, J.A. (1990). Dopamine receptor agonists: selectivity and dopamine D1 receptor efficacy. Eur. J. Pharmacol. *188*, 335–347.

Ballesteros, J.A., and Weinstein, H. (1995). Integrated methods for the construction of three-dimensional models and computational probing of structure-function relations in G protein-coupled receptors. In Methods in Neurosciences, S.C. Sealfon, ed. (Elsevier), pp. 366–428.

Beaulieu, J.M., and Gainetdinov, R.R. (2011). The physiology, signaling, and pharmacology of dopamine receptors. Pharmacol. Rev. *63*, 182–217.

Beninger, R.J., and Miller, R. (1998). Dopamine D1-like receptors and reward-related incentive learning. Neurosci. Biobehav. Rev. *22*, 335–345.

Butini, S., Nikolic, K., Kassel, S., Brückmann, H., Filipic, S., Agbaba, D., Gemma, S., Brogi, S., Brindisi, M., Campiani, G., and Stark, H. (2016). Polypharmacology of dopamine receptor ligands. Prog. Neurobiol. *142*, 68–103.

Carpenter, B., Nehmé, R., Warne, T., Leslie, A.G., and Tate, C.G. (2016). Structure of the adenosine A(2A) receptor bound to an engineered G protein. Nature *536*, 104–107.

Chen, V.B., Arendall, W.B., 3rd, Headd, J.J., Keedy, D.A., Immormino, R.M., Kapral, G.J., Murray, L.W., Richardson, J.S., and Richardson, D.C. (2010). MolProbity: all-atom structure validation for macromolecular crystallography. Acta Crystallogr. D Biol. Crystallogr. *66*, 12–21.

Chien, E.Y., Liu, W., Zhao, Q., Katritch, V., Han, G.W., Hanson, M.A., Shi, L., Newman, A.H., Javitch, J.A., Cherezov, V., and Stevens, R.C. (2010). Structure of the human dopamine D3 receptor in complex with a D2/D3 selective antagonist. Science *330*, 1091–1095.

Chun, E., Thompson, A.A., Liu, W., Roth, C.B., Griffith, M.T., Katritch, V., Kunken, J., Xu, F., Cherezov, V., Hanson, M.A., and Stevens, R.C. (2012). Fusion partner toolchest for the stabilization and crystallization of G protein-coupled receptors. Structure *20*, 967–976.

Conroy, J.L., Free, R.B., and Sibley, D.R. (2015). Identification of G protein-biased agonists that fail to recruit β-arrestin or promote internalization of the D1 dopamine receptor. ACS Chem. Neurosci. *6*, 681–692.

De Keyser, J., De Backer, J.P., Wilczak, N., and Herroelen, L. (1995). Dopamine agonists used in the treatment of Parkinson's disease and their selectivity for the D1, D2, and D3 dopamine receptors in human striatum. Prog. Neuropsychopharmacol. Biol. Psychiatry *19*, 1147–1154.

Di Chiara, G., and Gessa, G.L. (1978). Pharmacology and neurochemistry of apomorphine. Adv. Pharmacol. Chemother. *15*, 87–160.

Di Chiara, G., Bassareo, V., Fenu, S., De Luca, M.A., Spina, L., Cadoni, C., Acquas, E., Carboni, E., Valentini, V., and Lecca, D. (2004). Dopamine and drug addiction: the nucleus accumbens shell connection. Neuropharmacology *47* (*Suppl 1*), 227–241.

Emsley, P., and Cowtan, K. (2004). Coot: model-building tools for molecular graphics. Acta Crystallogr. D Biol. Crystallogr. *60*, 2126–2132.

Fan, L., Tan, L., Chen, Z., Qi, J., Nie, F., Luo, Z., Cheng, J., and Wang, S. (2020). Haloperidol bound D_2 dopamine receptor structure inspired the discovery of subtype selective ligands. Nat. Commun. *11*, 1074.

García-Nafría, J., Lee, Y., Bai, X., Carpenter, B., and Tate, C.G. (2018). Cryo-EM structure of the adenosine A_{2A} receptor coupled to an engineered heterotrimeric G protein. eLife *7*, e35946.

Giros, B., Sokoloff, P., Martres, M.P., Riou, J.F., Emorine, L.J., and Schwartz, J.C. (1989). Alternative splicing directs the expression of two D2 dopamine receptor isoforms. Nature *342*, 923–926.

Hall, A., Provins, L., and Valade, A. (2019). Novel Strategies To Activate the Dopamine D_1 Receptor: Recent Advances in Orthosteric Agonism and Positive Allosteric Modulation. J. Med. Chem. *62*, 128–140.

Heymann, J.B. (2018). Guidelines for using Bsoft for high resolution reconstruction and validation of biomolecular structures from electron micrographs. Prot. Sci. *27*, 159–171.

Kang, Y., Kuybeda, O., de Waal, P.W., Mukherjee, S., Van Eps, N., Dutka, P., Zhou, X.E., Bartesaghi, A., Erramilli, S., Morizumi, T., et al. (2018). Cryo-EM structure of human rhodopsin bound to an inhibitory G protein. Nature *558*, 553–558.

Koehl, A., Hu, H., Maeda, S., Zhang, Y., Qu, Q., Paggi, J.M., Latorraca, N.R., Hilger, D., Dawson, R., Matile, H., et al. (2018). Structure of the μ-opioid receptor-G_i protein complex. Nature *558*, 547–552.

Kostrzewa, R.M., Wydra, K., Filip, M., Crawford, C.A., McDougall, S.A., Brown, R.W., Borroto-Escuela, D.O., Fuxe, K., and Gainetdinov, R.R. (2018). Dopamine D_2 Receptor Supersensitivity as a Spectrum of Neurotoxicity and Status in Psychiatric Disorders. J. Pharmacol. Exp. Ther. *366*, 519–526.

Kroeze, W.K., Sassano, M.F., Huang, X.P., Lansu, K., McCorvy, J.D., Giguère, P.M., Sciaky, N., and Roth, B.L. (2015). PRESTO-Tango as an open-source resource for interrogation of the druggable human GPCRome. Nat. Struct. Mol. Biol. *22*, 362–369.

Lanau, F., Zenner, M.T., Civelli, O., and Hartman, D.S. (1997). Epinephrine and norepinephrine act as potent agonists at the recombinant human dopamine D4 receptor. J. Neurochem. *68*, 804–812.

Lee, S.M., Kant, A., Blake, D., Murthy, V., Boyd, K., Wyrick, S.J., and Mailman, R.B. (2014). SKF-83959 is not a highly-biased functionally selective D1 dopamine receptor ligand with activity at phospholipase C. Neuropharmacology *86*, 145–154.

Lemon, N., and Manahan-Vaughan, D. (2006). Dopamine D1/D5 receptors gate the acquisition of novel information through hippocampal long-term potentiation and long-term depression. J. Neurosci. *26*, 7723–7729.

Liang, Y.-L., Zhao, P., Draper-Joyce, C., Baltos, J.-A., Glukhova, A., Truong, T.T., May, L.T., Christopoulos, A., Wootten, D., Sexton, P.M., and Furness, S.G.B. (2018). Dominant Negative G Proteins Enhance Formation and Purification of Agonist-GPCR-G Protein Complexes for Structure Determination. ACS Pharmacol. Transl. Sci. *1*, 12–20.

Liu, W., Wacker, D., Gati, C., Han, G.W., James, D., Wang, D., Nelson, G., Weierstall, U., Katritch, V., Barty, A., et al. (2013). Serial femtosecond crystallography of G protein-coupled receptors. Science *342*, 1521–1524.

Liu, P., Jia, M.Z., Zhou, X.E., De Waal, P.W., Dickson, B.M., Liu, B., Hou, L., Yin, Y.T., Kang, Y.Y., Shi, Y., et al. (2016). The structural basis of the dominant negative phenotype of the Gαi1β1γ2 G203A/A326S heterotrimer. Acta Pharmacol. Sin. *37*, 1259–1272.

Mastronarde, D.N. (2005). Automated electron microscope tomography using robust prediction of specimen movements. J. Struct. Biol. *152*, 36–51.

Masureel, M., Zou, Y., Picard, L.P., van der Westhuizen, E., Mahoney, J.P., Rodrigues, J.P.G.L.M., Mildorf, T.J., Dror, R.O., Shaw, D.E., Bouvier, M., et al. (2018). Structural insights into binding specificity, efficacy and bias of a β_2AR partial agonist. Nat. Chem. Biol. *14*, 1059–1066.

McNab, F., Varrone, A., Farde, L., Jucaite, A., Bystritsky, P., Forssberg, H., and Klingberg, T. (2009). Changes in cortical dopamine D1 receptor binding associated with cognitive training. Science *323*, 800–802.

Missale, C., Nash, S.R., Robinson, S.W., Jaber, M., and Caron, M.G. (1998). Dopamine receptors: from structure to function. Physiol. Rev. *78*, 189–225.

Monsma, F.J., Jr., McVittie, L.D., Gerfen, C.R., Mahan, L.C., and Sibley, D.R. (1989). Multiple D2 dopamine receptors produced by alternative RNA splicing. Nature *342*, 926–929.

Neumeyer, J.L., Kula, N.S., Bergman, J., and Baldessarini, R.J. (2003). Receptor affinities of dopamine D1 receptor-selective novel phenylbenzazepines. Eur. J. Pharmacol. *474*, 137–140.

Parkes, J.D., Marsden, C.D., Donaldson, I., Galea-Debono, A., Walters, J., Kennedy, G., and Asselman, P. (1976). Bromocriptine treatment in Parkinson's disease. J. Neurol. Neurosurg. Psychiatry *39*, 184–193.

Pettersen, E.F., Goddard, T.D., Huang, C.C., Couch, G.S., Greenblatt, D.M., Meng, E.C., and Ferrin, T.E. (2004). UCSF Chimera–a visualization system for exploratory research and analysis. J. Comput. Chem. *25*, 1605–1612.

Pettersen, E.F., Goddard, T.D., Huang, C.C., Meng, E.C., Couch, G.S., Croll, T.I., Morris, J.H., and Ferrin, T.E. (2021). UCSF ChimeraX: Structure visualization for researchers, educators, and developers. Protein Sci. *30*, 70–82.

Rasmussen, S.G., Choi, H.J., Fung, J.J., Pardon, E., Casarosa, P., Chae, P.S., Devree, B.T., Rosenbaum, D.M., Thian, F.S., Kobilka, T.S., et al. (2011a). Structure of a nanobody-stabilized active state of the β(2) adrenoceptor. Nature *469*, 175–180.

Rasmussen, S.G., DeVree, B.T., Zou, Y., Kruse, A.C., Chung, K.Y., Kobilka, T.S., Thian, F.S., Chae, P.S., Pardon, E., Calinski, D., et al. (2011b). Crystal structure of the β2 adrenergic receptor-Gs protein complex. Nature *477*, 549–555.

Reichmann, H., Bilsing, A., Ehret, R., Greulich, W., Schulz, J.B., Schwartz, A., and Rascol, O. (2006). Ergoline and non-ergoline derivatives in the treatment of Parkinson's disease. J. Neurol. *253* (*Suppl 4*), IV36–IV38.

Ring, A.M., Manglik, A., Kruse, A.C., Enos, M.D., Weis, W.I., Garcia, K.C., and Kobilka, B.K. (2013). Adrenaline-activated structure of β2-adrenoceptor stabilized by an engineered nanobody. Nature *502*, 575–579.

Rohou, A., and Grigorieff, N. (2015). CTFFIND4: Fast and accurate defocus estimation from electron micrographs. J. Struct. Biol. *192*, 216–221.

Roth, B.L., Sheffler, D.J., and Kroeze, W.K. (2004). Magic shotguns versus magic bullets: selectively non-selective drugs for mood disorders and schizophrenia. Nat. Rev. Drug Discov. *3*, 353–359.

Sanchez-Garcia, R., Gomez-Blanco, J., Cuervo, A., Carazo, J., Sorzano, C., and Vargas, J. (2020). DeepEMhancer: a deep learning solution for cryo-EM volume post-processing. bioRxiv. https://doi.org/10.1101/2020.06.12.148296.

Sánchez-Soto, M., Bonifazi, A., Cai, N.S., Ellenberger, M.P., Newman, A.H., Ferré, S., and Yano, H. (2016). Evidence for Noncanonical Neurotransmitter Activation: Norepinephrine as a Dopamine D2-Like Receptor Agonist. Mol. Pharmacol. *89*, 457–466.

Steyaert, J., and Kobilka, B.K. (2011). Nanobody stabilization of G protein-coupled receptor conformational states. Curr. Opin. Struct. Biol. *21*, 567–572.

Vass, M., Podlewska, S., de Esch, I.J.P., Bojarski, A.J., Leurs, R., Kooistra, A.J., and de Graaf, C. (2019). Aminergic GPCR-Ligand Interactions: A Chemical and Structural Map of Receptor Mutation Data. J. Med. Chem. *62*, 3784–3839.

Vijayraghavan, S., Wang, M., Birnbaum, S.G., Williams, G.V., and Arnsten, A.F. (2007). Inverted-U dopamine D1 receptor actions on prefrontal neurons engaged in working memory. Nat. Neurosci. *10*, 376–384.

Volkow, N.D., and Morales, M. (2015). The Brain on Drugs: From Reward to Addiction. Cell *162*, 712–725.

Wang, S., Wacker, D., Levit, A., Che, T., Betz, R.M., McCorvy, J.D., Venkatakrishnan, A.J., Huang, X.P., Dror, R.O., Shoichet, B.K., and Roth, B.L. (2017). D_4 dopamine receptor high-resolution structures enable the discovery of selective agonists. Science *358*, 381–386.

Wang, S., Che, T., Levit, A., Shoichet, B.K., Wacker, D., and Roth, B.L. (2018). Structure of the D2 dopamine receptor bound to the atypical antipsychotic drug risperidone. Nature *555*, 269–273.

Xiao, P., Yan, W., Gou, L., Zhong, Y.-N., Kong, L., Wu, C., Wen, X., Yuan, Y., and Cao, S. (2021). Ligand recognition and allosteric regulationof DRD1-Gs signaling complexes. Cell *184*.

Xing, C., Zhuang, Y., Xu, T.H., Feng, Z., Zhou, X.E., Chen, M., Wang, L., Meng, X., Xue, Y., Wang, J., et al. (2020). Cryo-EM Structure of the Human Cannabinoid Receptor CB2-G_i Signaling Complex. Cell *180*, 645–654.e13.

Yin, J., Chen, K.M., Clark, M.J., Hijazi, M., Kumari, P., Bai, X.C., Sunahara, R.K., Barth, P., and Rosenbaum, D.M. (2020). Structure of a D2 dopamine receptor-G-protein complex in a lipid membrane. Nature *584*, 125–129.

Zhang, K. (2016). Gctf: Real-time CTF determination and correction. J. Struct. Biol. *193*, 1–12.

Zheng, S.Q., Palovcak, E., Armache, J.P., Verba, K.A., Cheng, Y., and Agard, D.A. (2017). MotionCor2: anisotropic correction of beam-induced motion for improved cryo-electron microscopy. Nat. Methods *14*, 331–332.

Zhuang, Y., Liu, H., Edward Zhou, X., Kumar Verma, R., de Waal, P.W., Jang, W., Xu, T.H., Wang, L., Meng, X., Zhao, G., et al. (2020). Structure of formylpeptide receptor 2-G_i complex reveals insights into ligand recognition and signaling. Nat. Commun. *11*, 885.

Zivanov, J., Nakane, T., Forsberg, B.O., Kimanius, D., Hagen, W.J., Lindahl, E., and Scheres, S.H. (2018). New tools for automated high-resolution cryo-EM structure determination in RELION-3. eLife *7*, e42166.

STAR★METHODS

KEY RESOURCES TABLE

REAGENT or RESOURCE	SOURCE	IDENTIFIER
Antibodies		
GP64-PE antibody	Expression systems	Cat# 97-201
Anti-hemagglutinin HRP conjugate	Sigma-Aldrich	Cat#A8592
Chemicals, peptides, and recombinant proteins		
SKF81297 hydrobromide	Tocris	Cat# 1447/10
SKF83959 hydrobromide	Tocris	Cat# 2074
Apomorphine hydrochloride	Tocris	Cat# 2073/50
Bromocriptine mesylate	TargetMol	Cat# T5842
Dopamine	Sigma-Aldrich	Cat# H8502
[^{3}H]-SCH23390	Perkin Elmer	Cat# NET930025UC
Lauryl maltose neopentyl glycol	Anatrace	Cat# NG310
n-dodecyl-β-D-maltoside (DDM)	Anatrace	Cat# D310S
Glyco-diosgenin (GDN)	Anatrace	Cat# GDN101
Cholesteryl Hemisuccinate	Anatrace	Cat# CH210
Digitonin	Biosynth	Cat# D-3200
ClonExpress II One Step Cloning Kit	Vazyme Biotech Co.,Ltd	Cat# C112
Protease Inhibitor Cocktail, EDTA-free	Bimake	Cat# B14003
Apyrase	New England Biolabs	Cat# M0398L
Nickel Sepharose resin	GE healthcare	Cat#17526801
Anti-Flag resin	Smart-Lifesciences	Cat# C20042002
FLAG peptide	Synpeptide Co Ltd	Custom Synthesis
ESF921 culture medium	Expression systems	Cat# 96-001-01
Talon resin	Takara	Cat# 635504
Dulbecco's Modified Eagle Medium (DMEM)	VWR	Cat# 45000-306
Fetal bovine serum (FBS)	VWR	Cat#97068-085
Penicillin/ Streptomycin	Invitrogen	Cat#15140-122
TransIT-2-2- Transfection Reagent	Mirus	Cat# MIR5400
Horse Radish Peroxidase (HRP) Substrate	ThermoFisher	Cat# 37069
Hanks' Balanced Salt Solution (HBSS)	Invitrogen	Cat# 14065-056
Glosensor Assay Reagent	Promega	Cat# E1290
Bright-Glo Luciferase Reagent	Promega	Cat# E2610
Critical commercial assays		
Bac-to-Bac Baculovirus Expression System	Invitrogen	Cat# A11098
pcDNA 3.1	Thermo Fisher	Cat#V79020
Glosensor Plasmid 22F	Promega	Cat#E2301
Deposited data		
D1R- SKF81297- G_s coordinates	This paper	PDB: 7JV5
D1R- SKF83959- G_s coordinates	This paper	PDB: 7JVP
D1R- apomorphine- G_s coordinates	This paper	PDB: 7JVQ
D2R-bromocriptine- G_i coordinates	This paper	PDB: 7JVR
D1R- SKF81297- G_s EM map	This paper	EMDB: EMD-22493
D1R- SKF83959- G_s EM map	This paper	EMDB: EMD-22509
D1R- apomorphine- G_s EM map	This paper	EMDB: EMD-22510

(*Continued on next page*)

Continued		
REAGENT or RESOURCE	SOURCE	IDENTIFIER
D2R-bromocriptine- G_i EM map	This paper	EMDB: EMD-22511
Experimental models: cell lines		
E. coli strain BL21 (DE3)	NEB	Cat# C2527
Spodoptera frugiperda Sf9 cells	Expression Systems	Cat# 94-001F
HEK293T cells	ATCC	Cat# CRL-11268
Recombinant DNA		
pFastbac-prolactin-FLAG-BN-D1R-H8	This paper	N/A
pFastbac-HA- FLAG-BRIL-D2R-H8	This paper	N/A
pFastbac- DN_$G_{\alpha s}$	This paper	N/A
pFastbac- DN_mini$G_{\alpha s}$	This paper	N/A
pFastbac- DN_$G_{\alpha i}$	This paper	N/A
pFastbac-H8-$G_{\beta 1}$	This paper	N/A
pFastbac-$G_{\gamma 2}$	This paper	N/A
pFastbac-GP67-scFv16-Tev-H8	This paper	N/A
Software and algorithms		
Clonemanager	Sci-Ed Software	http://www.scied.com/pr_cmpro.htm
Prism 8	GraphPad	https://www.graphpad.com/scientific-software/prism/
SerialEM	Mastronarde, 2005	https://bio3d.colorado.edu/SerialEM/
MotionCor2	(Zheng et al., 2017)	https://msg.ucsf.edu/em/software/motioncor2.html
Relion 3.0	Zivanov, et al., 2018	https://www3.mrc-lmb.cam.ac.uk/relion/index.php/Download_%26_install
UCSF Chimera	Pettersen et al., 2004	https://www.cgl.ucsf.edu/chimera/
UCSF ChimeraX	(Pettersen et al., 2021)	https://www.cgl.ucsf.edu/chimerax/
Phenix	(Adams et al., 2010)	https://www.phenix-online.org/
MolProbity	Chen et al., 2010	http://molprobity.biochem.duke.edu/
Coot	Emsley and Cowtan, 2004	https://www2.mrc-lmb.cam.ac.uk/personal/pemsley/coot/
PyMol 2.3	Schrödinger	https://pymol.org/2/
Adobe Illustrator CC	Adobe	https://www.adobe.com
Other		
Quantifoil R1.2/1.3 300-mesh Gold grids	Quantifoil	https://www.emsdiasum.com/microscopy/products/grids/quantifoil.aspx
Superdex 200 Increase column	GE healthcare	Cat#28990944

RESOURCE AVAILABILITY

Lead contact

Further information and requests for reagents may be directed and will be fulfilled by the Lead Contact, H. Eric Xu (eric.xu@simm.ac.cn).

Materials availability

All unique or stable reagents generated in this study are available from the Lead Contact without restriction. Plasmids and strains are available from the authors upon request.

Data and software availability

The cryo-EM density maps of D1R-G_s complexes and D2R-G_i complex have been deposited in the Electron Microscopy Data Bank under the accession numbers EMD-22493 for D1R-SKF81297-G_s, EMD-22509 for D1R-SKF83959 -G_s, EMD-22510 for D1R-apomorphine-G_s and EMD-22511 for D2R-bromocriptine-G_i. Structure coordinates have been deposited in the Protein Data Bank

under the accession codes PDB 7JV5, PDB 7JVP and PDB 7JVQ for SKF81297-, SKF83959- and apomorphine-bound D1R-G_s complex, respectively, and PDB 7JVR for bromocriptine-bound D2R-G_i complex. All other data are available from the main text and supplemental data. The softwares used were available from the Key resources table.

EXPERIMENTAL MODEL AND SUBJECT DETAILS

Two kinds of eukaryotic cell lines, *Spodoptera frugiperda* (Sf9, Expression systems) cells and HEK293T cells (ATCC), were used for recombinant protein expression and functional studies, respectively. Sf9 cells were grown in ESF 921 medium (Expression systems) at 27°C, 120 rpm. HEK293T cells were grown in humidified 37°C incubator in condition of 5% CO_2 using medium supplemented with 100 I.U. / mL penicillin and 100 mg / mL streptomycin (Invitrogen). The medium for human cell lines HEK293T was DMEM (VWR) containing 10% fetal bovine serum (FBS, VWR).

METHOD DETAILS

Constructs

The full-length gene sequence of wild-type human D1R was synthesized and subcloned into pFastBac (Thermo Fisher) vector with an N-terminal FLAG tag followed by a fragment of β_2AR N-terminal tail region (BN, hereafter) as fusion protein, along with a C-terminal 8 × His tag to facilitate the protein expression and purification. The D1R sequence had no additional mutations or loop deletions. A TEV cleavage site was inserted between BN and D1R gene sequences. The prolactin precursor sequence was placed into the N terminus before the FLAG tag as signaling peptide to increase D1R cell membrane localization and increase D1R expression (Figure S1A). For structure determination of the D1R-G_s-SKF81297 and D1R-G_s-SKF83959 complexes, a dominant-negative form of human $G_{\alpha s}$ (DN_$G_{\alpha s}$) was constructed by site-directed mutagenesis to incorporate mutations G226A and A366S to decrease the affinity of nucleotide binding to the heterotrimer $G_{\alpha\beta\gamma}$ complex (Liu et al., 2016). To obtain a well-performed D1R-G_s-apomorphine complex, a mini$G_{\alpha s}$ format including mutations G226A and A366S (DN_mini$G_{\alpha s}$) was constructed by removing the α-helical domain of $G_{\alpha s}$ and introducing mutations according to the previously reported mini$G_{\alpha s}$ sequence (Carpenter et al., 2016; García-Nafría et al., 2018) (Figure S1B). All the three G_s protein complex components, DN_$G_{\alpha s}$/ DN_mini $G_{\alpha s}$, rat $G_{\beta 1}$ and bovine $G_{\gamma 2}$, were cloned into pFastbac vector separately with a His8 tag introduced into the N terminus of $G_{\beta 1}$ to aid purification. For structure determination of the D2R-G_i-bromocriptine complex, the full-length gene sequence of wild-type human D2R was cloned into pFastBac vector with an N-terminal haemagglutinin (HA) signaling peptide sequence followed by a FLAG tag, a His8 tag and a BRIL to facilitate expression and purification (Figure S1H). Four dominant-negative mutations, S47N, G203A, E245A, A326S, were incorporated into human $G_{\alpha i}$ (DN_$G_{\alpha i}$) to reduce the nucleotide binding (Liang et al., 2018). Human DN_$G_{\alpha i}$, rat $G_{\beta 1}$, bovine $G_{\gamma 2}$ and scFv16 antibody fragment (Koehl et al., 2018) were cloned into pFastBac vector.

Expression, complex formation and purification

D1R, DN_$G_{\alpha s}$/ DN_mini$G_{\alpha s}$, His8-tagged $G_{\beta 1}$ and $G_{\gamma 2}$ were co-expressed in Sf9 insect cells (Expression System) while the D2R, DN_$G_{\alpha i}$, $G_{\beta 1}$, $G_{\gamma 2}$, and scFv16 were co-expressed in Hi5 insect cells (Invitrogen), using the Bac-to-Bac baculovirus expression system (Thermo Fisher). Cell cultures were grown in ESF 921 serum-free medium (Expression Systems) to a density of 4 × 10^6 cells/mL. For the expression of the D1R-G_s/miniG_s complex, Sf9 cells were infected with the four types of baculoviruses: D1R, DN_$G_{\alpha s}$/ DN_miniG_s, His8-tagged $G_{\beta 1}$ and $G_{\gamma 2}$ at the ratio of 1:1:1:1. For the expression of the D2R-G_i complex, Hi5 cells were infected with the five types of baculoviruses: D2R, DN_$G_{\alpha i}$, $G_{\beta 1}$, $G_{\gamma 2}$ and scFv16. After infected by 48 h, the cells were harvested by centrifugation at 1300 × g (Thermo Fisher, H12000) for 20 min and kept frozen at −80°C for further usage.

For the purification of both the D1R- SKF81297-G_s complex and the D1R-SKF83959-G_s complex, cell pellets from 2L culture were thawed at room temperature and resuspended in low salt buffer containing 20 mM HEPES pH 7.2, 50 mM NaCl, 5 mM $CaCl_2$, 5 mM $MgCl_2$, 0.3 mM TECP, protease inhibitor cocktail (Bimake, 1 mL/ 100 mL suspension). The D1R-G_s complexes were formed on membrane in the presence of 5 μM SKF ligands (SKF81297 or SKF83959) (Tocris) and treated with apyrase (25 mU mL^{-1}, NEB), followed by incubation for 1.5 h at room temperature. Cell membranes were collected by ultra-centrifugation at 100,000 x g for 35 min. The membranes were then resuspended and solubilized in buffer containing 20 mM HEPES, pH 7.2, 100 mM NaCl, 25 mM imidazole, 5 mM $CaCl_2$, 10% glycerol, 0.3 mM TCEP, 0.5% (w/v) dodecyl-β-D-maltoside (DDM, Anatrace), 0.1% (w/v) cholesteryl hemisuccinate TRIS salt (CHS, Anatrace), 0.025%(w/v) digitonin (Biosynth), 2.5 μM SKF ligands, supplemented with 25 mU mL^{-1} apyrase and 10 μg/mL Nb35 for 3 h at 4°C. The supernatant was isolated by centrifugation at 100,000 × g for 45 min and then incubated overnight at 4°C with pre-equilibrated Nickel-NTA resin. After batch binding, the nickel resin with immobilized protein complex was manually loaded onto a gravity flow column. The nickel resin was washed with 10 column volumes of 20 mM HEPES, pH 7.2, 100 mM NaCl, 25 mM imidazole, 0.3 mM TCEP, 0.1% DDM (w/v), 0.02% CHS (w/v), 0.025% digitonin (w/v), 2.5 μM SKF ligands and eluted with the same buffer plus 300 mM imidazole. The Ni-NTA eluate was further incubated by batch binding to 2.5 mL FLAG resin (Smart-Lifesciences) for 2 h at 4°C. Detergent was exchanged on FLAG resin by two washing steps in 20 mM HEPES, pH 7.2, 100 mM NaCl, 0.3 mM TCEP, 2.5 μM SKF ligands supplemented with different detergents: first 0.02% DDM, 0.004% CHS, 0.05% digitonin, and then 0.05% digitonin for 10 column volumes each. Subsequently, the material bound to FLAG resin was eluted in detergent buffer containing 20 mM HEPES, pH 7.2, 100 mM NaCl, 0.3 mM TCEP, 5 μM SKF ligands, 0.05% digitonin, 200 μg/μL FLAG peptide.

For the purification of D1R-apomorphine-miniG$_s$, cell pellets from 1 L culture were thawed at room temperature and resuspended in buffer containing 20 mM HEPES pH 7.2, 75 mM NaCl, 5 mM $CaCl_2$, 5 mM $MgCl_2$, 10% Glycerol, 0.3 mM TECP, protease inhibitor cocktail (Bimake, 1 mL/ 100 mL suspension). The protein complex was formed on membrane by adding 50 μM apomorphine (Tocris), 10 μg/mL Nb35 and treated with apyrase (25 mU mL^{-1}, NEB). After incubation for 1.5 h at room temperature, the membrane in suspension was solubilized by 0.5% (w/v) DDM, 0.1% (w/v) CHS, 0.025% (w/v) digitonin for 3 hours at 4°C. The isolated supernatant was incubated for 2 hours at 4°C directly with pre-equilibrated FLAG resin (Smart-Lifesciences). Detergent was exchanged on FLAG resin by three washing steps in 20 mM HEPES, pH 7.2, 100 mM NaCl, 0.3 mM TCEP, 10 μM apomorphine supplemented with different detergents: first 0.1% DDM, 0.02% CHS, 0.025% digitonin, then 0.02% DDM, 0.004% CHS, 0.05% digitonin, and finally 0.05% digitonin for 10 column volumes, each. The protein complex was then eluted in buffer containing 20 mM HEPES, pH 7.2, 100 mM NaCl, 0.3 mM TCEP, 10 μM apomorphine, 0.05% digitonin, 200 μg/μL FLAG peptide.

Released protein was further concentrated to 0.5 mL using centrifugal filters with a 100 kDa molecular weight cut-off (ThermoFisher) and then loaded onto a Superdex 200 10/300 GL Increase column (GE Healthcare) pre-equilibrated with buffer containing 20 mM HEPES, pH 7.2, 100 mM NaCl, 0.05% digitonin, 0.1 mM TCEP, 2.5 μM SKF compounds or 10 μM apomorphine. The fractions of monomeric complex were pooled and concentrated for electron microscopy experiments.

For the purification of the D2R-bromocriptine-G$_i$-scFv16 complex, cell pellets from 2 L culture were resuspended in a low salt buffer containing 20 mM HEPES, pH 7.4, 100 mM NaCl, 5 mM $MgCl_2$, 5 mM $CaCl_2$, 25 mU/mL Apyrase, protease inhibitor cocktail and 10 μM bromocriptine (TargetMol). The cell pellets were homogenized and incubated at room temperature for 1 h. The sample was centrifuged at 65,000 × g for 30 min, then the membranes were resuspended in buffer containing 20 mM HEPES, pH 7.4, 100 mM NaCl, protease inhibitor cocktail, 10 mM imidazole, 0.5% Lauryl Maltose Neopentyl Glycol (LMNG, Anatrace), 0.1% CHS and 10 μM bromocriptine. The membranes were solubilized at 4°C for 2 h, then the supernatant was collected by centrifugation and incubated with TALON resin (Takara Clontech) at 4°C for 3 h. The resin was washed with 10 column volumes of Wash Buffer I containing 20 mM HEPES, pH 7.4, 100 mM NaCl, 15 mM imidazole, 0.1% LMNG, 0.02% CHS, 10 μM bromocriptine and with 10 column volumes of Wash Buffer II containing 20 mM HEPES, pH 7.4, 100 mM NaCl, 20 mM imidazole, 0.01% LMNG, 0.005% GDN (Anatrace), 0.003% CHS, 10 μM bromocriptine. The complex was then eluted with 5 column volumes of Elution Buffer containing 20 mM HEPES, pH 7.4, 100 mM NaCl, 250 mM imidazole, 0.01% LMNG, 0.005% GDN, 0.003% CHS and 10 μM bromocriptine. The complex was concentrated to 0.5 mL using centrifugal filters with a 100 kDa molecular weight cut-off (ThermoFisher) and loaded onto a Superdex 200 10/300 GL increase column pre-equilibrated with Size Buffer containing 20 mM HEPES, pH 7.4, 100 mM NaCl, 0.00075% LMNG, 0.00025% GDN, 0.00015% CHS, and 10 μM bromocriptine. The fractions of monomeric complex were collected and concentrated to 20 mg mL^{-1} for electron microscopy experiments.

Cryo-EM grid preparation and data collection

For the cryo-EM grids preparation, 3 μL purified D1R-SKF81297-G$_s$-Nb35 complex at the concentration about 27 mg mL^{-1}, D1R-SKF83959-G$_s$-Nb35 complex at the concentration about 23 mg mL^{-1}, D1R-apomorphine-miniG$_s$-Nb35 complex at the concentration of 35 mg mL^{-1}, and D2R-bromocriptine-G$_i$-scFv16 complex at the concentration of 20 mg mL^{-1} were applied individually to a glow-discharged holey carbon EM grid (Quantifoil, Au200 R1.2/1.3) in a Vitrobot chamber (FEI Vitrobot Mark IV). Protein concentration was determined by absorbance at 280 nm using a Nanodrop 2000 Spectrophotometer (Thermo Fisher Scientific). The Vitrobot chamber was set to 100% humidity at 4°C. The sample-coated grids were blotted before plunge-freezing into liquid ethane and stored in liquid nitrogen for data collection.

For D1R-SKF81297-G$_s$-Nb35 complex and D1R-apomorphine-miniG$_s$-Nb35 complex, automatic data collection was performed on a FEI Titan Krios equipped with a Gatan K2 Summit direct electron detector in the Center of Cryo-Electron Microscopy, Zhejiang University (Hangzhou, China). The microscope was operated at 300 kV accelerating voltage, at a nominal magnification of 29,000 × in counting mode, corresponding to a pixel size of 1.014 Å. For the dataset of D1R-SKF81297-G$_s$-Nb35 complex, a total of 2,000 movies were obtained at a dose rate of about 8 electrons per Å^2 per second with a defocus ranging from −0.5 to −3.0 μm. The total exposure time was 8 s and intermediate frames were recorded in 0.2 s intervals, resulting in an accumulated dose of 64 electrons per Å^2 and a total of 40 frames per micrograph. In the dataset of D1R-apomorphine-G$_s$-Nb35 complex, a total of 2188 movies were obtained at a dose rate of about 8.0 electrons per Å^2 per second with a defocus ranging from −0.5 to −3.0 μm. The total exposure time was 8 s and intermediate frames were recorded in 0.2 s intervals, resulting in an accumulated dose of 64 electrons per Å^2 and a total of 40 frames per micrograph.

For the D1R-SKF83959-G$_s$-Nb35 complex and the D2R-bromocriptine-G$_i$-scFv16 complex, automatic data collection was performed on a FEI Titan Krios at 300 kV in Cryo-Electron Microscopy Research Center, Shanghai Institute of Materia Medica, Chinese Academy of Sciences (Shanghai, China). The microscope was operated at a nominal magnification of 81,000 × in counting mode, corresponding to pixel size of micrograph at 1.045 Å. A total of 3,057 movies for the dataset of D1R-SKF83959-G$_s$-Nb35 complex and 5,100 movies for the dataset of D2R-bromocriptine-G$_i$-scFv16 complex were collected by a Gatan K3 Summit direct electron detector with a Gatan energy filter (operated with a slit width of 20 eV) (GIF) using the SerialEM software (Mastronarde, 2005). The images were recorded at a dose rate of about 26.7 e/Å^2/s with a defocus ranging from −0.5 to −3.0 μm. The total exposure time was 3 s and intermediate frames were recorded in 0.083 s intervals, resulting in a total of 36 frames per micrograph.

Image processing and map reconstruction

Dose-fractionated image stacks were subjected to beam-induced motion correction using MotionCor2.1 (Zheng et al., 2017). A sum of all frames, filtered according to the exposure dose, in each image stack was used for further processing. Contrast transfer function parameters for each micrograph were determined by Gctf v1.06 (Zhang, 2016). Particle selection and 2D and 3D classifications were performed on a binned dataset with a pixel size of 2.028 Å using RELION-3.0-beta2(3) (Zivanov et al., 2018). For the D1R-SKF81297-G_s dataset, auto-picking yielded 1,197,896 particle projections that were subjected to reference-free 2D classification to discard false positive particles or particles categorized in poorly defined classes, producing 787,504 particle projections for further processing. This subset of particle projections was subjected to a round of maximum-likelihood-based three-dimensional classification with a pixel size of 2.028 Å. A selected subset containing 645,131 projections was used to obtain the final map using a pixel size of 1.014 Å. After the last round of refinement, the final map had an indicated global resolution of 3.0 Å at a Fourier shell correlation (FSC) of 0.143. For the D1R-apomorphine-miniG_s dataset, automated particle selection produced 1,668,950 particles, which were subjected to reference-free 2D classification to discard particles in poorly defined classes. The map of PTH1R-G_s complex (EMDB: EMD-0410) low-pass filtered to 40 Å was used as an initial reference model for 2 rounds of 3D classification, resulting in two well-defined subsets with 363,884 projections. Further 3D classifications focusing the alignment on the receptor, produced one good subsets accounting for 212,652 particles, which were subsequently subjected to 3D refinement and Bayesian polishing with a pixel size of 1.014. The final refinement with frames 1-20 generated a map with an indicated global resolution of 3.0 Å at a Fourier shell correlation of 0.143.

For D1R-SKF83959-G_s-Nb35 complex, movie stacks were subjected to beam-induced motion correction using MotionCor2.1 (Zheng et al., 2017). Contrast transfer function parameters for each micrograph were determined by Ctffind4 (Rohou and Grigorieff, 2015). Particle selection, 2D and 3D classifications were performed on a binned dataset with a pixel size of 2.09 Å using RELION-3.0-beta2 (Zivanov et al., 2018). About 2000 particles were manually selected and subjected to 2D classification. Representative averages were picked as template for auto-picking. The auto-picking process produced 2,034,626 particles, which were subjected to 2D classifications. An initial model was generated by RELION-3.0 and served as initial reference map for four rounds of 3D classifications, resulting in two well-defined subsets with 679,728 particles. Subsequent 3D refinement and postprocess generated a map with an indicated global resolution of 2.9 Å at a Fourier shell correlation of 0.143.

For the D2R-bromocriptine-G_i-scFv16 complex, movie stacks were subjected to beam-induced motion correction using MotionCor2.1 (Zheng et al., 2017). Contrast transfer function parameters for each micrograph were determined by Ctffind4 (Rohou and Grigorieff, 2015). Particle selection, 2D and 3D classifications were performed on a binned dataset with a pixel size of 2.09 Å using RELION-3.0-beta2 (Zivanov et al., 2018). Auto-pick yielded 7,846,162 particles, which were subjected to 2D classifications. An initial model was generated by RELION-3.0 and served as initial reference map for three rounds of 3D classifications, resulting in two well-defined subsets with 632,558 particles. A map generated by 3D refinement was subsequent post-processed in DeepEMhancer (Sanchez-Garcia et al., 2020) and the map indicated a global resolution of 2.8 Å at a Fourier shell correlation of 0.143. Local resolution was determined using the Bsoft package with half maps as input maps (Heymann, 2018).

Structure model building and refinement

The structure of β_2AR-G_s complex (PDB: 3SN6) was used as initial model for model rebuilding and refinement against the electron microscopy maps of D1R-G_s complexes. The structure of haloperidol bound D2R (6LUQ) and the structure of the G_i part of the rhodopsin-G_i complex (6CMO) were used as initial models for model building of the D2R-bromocriptine-G_i-scFv16 complex. The initial models were docked into the electron microscopy density maps using Chimera (Pettersen et al., 2004) followed by iterative manual adjustment and rebuilding in COOT (Emsley and Cowtan, 2004). Real space refinement and reciprocal space refinement were performed using Phenix programs (Adams et al., 2010). The model statistics were validated using MolProbity (Chen et al., 2010). Structure figures were prepared in Chimera and PyMOL (https://pymol.org/2/). The final refinement statistics are provided in Table S1. The extent of any model overfitting during refinement was measured by refining the final model against one of the half-maps and by comparing the resulting map versus model FSC curves with the two half-maps and the full model.

Radioligand binding assays

Binding assays were performed using membranes from HEK293T (ATCC CRL-11268) cells transiently expressing wild-type D1R or D1R mutants. Binding assays were set up in 96-well plates in standard binding buffer (50 mM HEPES, 50 mM NaCl, 5 mM $MgCl_2$, 0.5 mM EDTA, pH 7.4). Saturation binding assays with 0.5-5 nM [^{3}H]-SCH23390 (Perkin-Elmer) in standard binding buffer were performed to determine equilibrium dissociation constant (Kd) and Bmax, whereas 10 μM final concentration of Butaclamol was used to define nonspecific binding. Reactions were incubated for 2 h at room temperature in the dark and terminated by rapid vacuum filtration onto chilled 0.3% PEI-soaked GF/A filters (Perkin-Elmer) followed by three quick washes with cold washing buffer (50 mM Tris HCl, pH 7.40). Radioactivity counts were determined using a Wallac Trilux MicroBeta counter (Perkin-Elmer). Results were analyzed using GraphPad Prism 8.4 (Graphpad Software Inc., San Diego, CA) using ''One site–Total and nonspecific binding.'' Competition assays were performed similar to saturation binding assays except that various concentrations of competitor were premixed with [^{3}H]-SCH23390 (Perkin-Elmer) near the pre-determined equilibrium dissociation constant (Kd) and then incubated for 2 h at room temperature in the dark with membranes from HEK293T (ATCC CRL-11268) cells transiently expressing wild-type D1R or D1R mu-

tants. Results were analyzed using GraphPad Prism 8.4 (Graphpad Software Inc., San Diego, CA) using either ''One site-Fit Ki'' or ''Two site-Fit Ki'' as determined when comparing values in GraphPad Prism 8.4.

Surface expression analysis

Surface expression determination of wild-type D1R and mutants was performed using HEK293T cells (ATCC CRL-11268) maintained in DMEM containing 10% (v/v) dialyzed FBS, 1 IU mL^{-1} Penicillin G, and 100 μg mL^{-1} Streptomycin. Cells were passed to 6-well plates (Genesee Scientific, Cat 25-106MP) and transfected using TransIT (Mirus Bio) and 0.4 μg of the given receptor. After at least 24 h, transfected cells were plated in polylysine-coated 96-well white clear bottom cell culture plates (Greiner Bio-One) in plating media (DMEM containing 1% (v/v) dialyzed FBS, 1 IU mL^{-1} Penicillin G, and 100 μg mL^{-1} Streptomycin) at a density of 20,000 cells in 200 μL per well and incubated overnight. The following day, media was aspirated and cells were washed twice with 200 μL of 1 × Phosphate Buffered Saline (PBS). Then 100 μL of 1 × PBS containing 5% (w/v) BSA was added to each well and incubated at RT. After 30 min, 100 μL of 1:10,000 anti-hemagglutinin HRP conjugate (Sigma-Aldrich Cat A8592) was added to each well. After an additional 30 min, media was aspirated and cells were washed twice with 200 μL of 1 × Phosphate Buffered Saline (PBS). Chemiluminescence was observed by the addition of 50 μL of HRP substrate (Thermo Fisher, Cat 37069) and counted using a Wallac Trilux MicroBeta counter (Perkin-Elmer). Chemiluminescence values were normalized to wild-type receptor and graphed as a percentage of wild-type using Graphpad Prism 8 (Graphpad Software Inc., San Diego, CA).

D1R G_S-mediated G_S-cAMP accumulation assay

D1R G_S-mediated G_S-cAMP accumulation assays with HEK293T (ATCC CRL-11268) were performed using cells transiently expressing human D1R and the cAMP biosensor GloSensor-22F (Promega). Cells were seeded (20 000 cells/35 μL/well) into white 384 clear-bottom, tissue culture plates in DMEM containing 1% (v/v) dialyzed fetal bovine serum (FBS). Next day, 3x drug dilutions were diluted in HBSS, 20 mM N-(2-hydroxyethyl) piperazine-N′-ethanesulfonic acid (HEPES), 0.3% (w/v) bovine serum albumin (BSA), 0.03% (w/v) ascorbic acid, pH 7.4. Media was decanted from 384 well plates and 20 μL of drug buffer (HBSS, 20 mM HEPES, pH 7.4) containing GloSensor reagent was added per well and allowed to equilibrate for at least 15 min at room temperature. Cells were then treated with 10 μL per well of 3 × drug using a FLIPR (Molecular Devices). After 15 min, G_s-cAMP accumulation was read on a TriLux Microbeta (PerkinElmer) plate counter. Data were analyzed using the sigmoidal log(agonist) versus dose response function built into GraphPad Prism 8.4.

Tango arrestin recruitment assay

Human DRD1 Tango constructs were designed and assays were performed as previously described (Kroeze et al., 2015; Liu et al., 2013). HTLA cells expressing TEV fused-β-Arrestin2 (kindly provided by Dr. Richard Axel, Columbia Univ.) were transfected with the 8 μg DRD1 Tango construct. After at least 16 h, cells were plated in DMEM supplemented with 1% (v/v) dialyzed FBS in poly-L-lysine coated 384-well white clear bottom cell culture plates at a density of 10,000-15,000 cells/well in a total of 40 μL. The cells were incubated for at least 6 h before receiving drug stimulation. Drug solutions were prepared in drug buffer (20 mM HEPES, 1 × HBSS, 0.3% BSA, pH 7.4) at 3 × and added to cells (20 μL per well) for overnight incubation. After at least 16 h, media and drug solutions were removed and 20 μL per well of diluted 1:20 BrightGlo reagent (Promega) was added. The plate was incubated for 20 min at room temperature in the dark before being counted using a TriLux Microbeta (PerkinElmer) plate counter. Results (relative luminescence units) were plotted as a function of drug concentration and analyzed using GraphPad Prism 8.4.

Figure preparation

The density maps were prepared in UCSF Chimera (https://www.cgl.ucsf.edu/chimera/) and UCSF ChimeraX (https://www.cgl.ucsf.edu/chimerax/). Structural comparison and alignment figures were prepared with PyMOL (https://pymol.org/2/).

QUANTIFICATION AND STATISTICAL ANALYSIS

For radioligand saturation binding assays, results were analyzed using GraphPad Prism 8.4 (Graphpad Software Inc., San Diego, CA) using ''One site–Total and nonspecific binding.'' For the radioligand competition binding assays, data were analyzed using GraphPad Prism 8.4 (Graphpad Software Inc., San Diego, CA) using either ''One site-Fit Ki'' or ''Two site-Fit Ki'' as determined when comparing values in GraphPad Prism 8.4. For surface expression levels of WT D1R and D1R mutants, chemiluminescence values were normalized to wild-type receptor and graphed as a percentage of wild-type using Graphpad Prism 8.4 (Graphpad Software Inc., San Diego, CA). The pEC_{50} values were calculated for individual experiments using the sigmoidal log(agonist) versus dose response function built into GraphPad Prism 8.4. Average Emax values for cAMP accumulation assay were determined from ''log(agonist) vs. response-Variable slope (four parameters)'' function in Graphpad Prism 8.4 software (Graphpad Software Inc., San Diego, CA). Average Emax and basal values for the β-arrestin recruitment Tango assays were determined from the highest and lowest concentrations of the respective compound. Data in the figures and tables are presented as mean values ± standard error of measurement (SEM) with the number of biological and technical replicates indicated in the figure and table legends.

Supplemental Figures

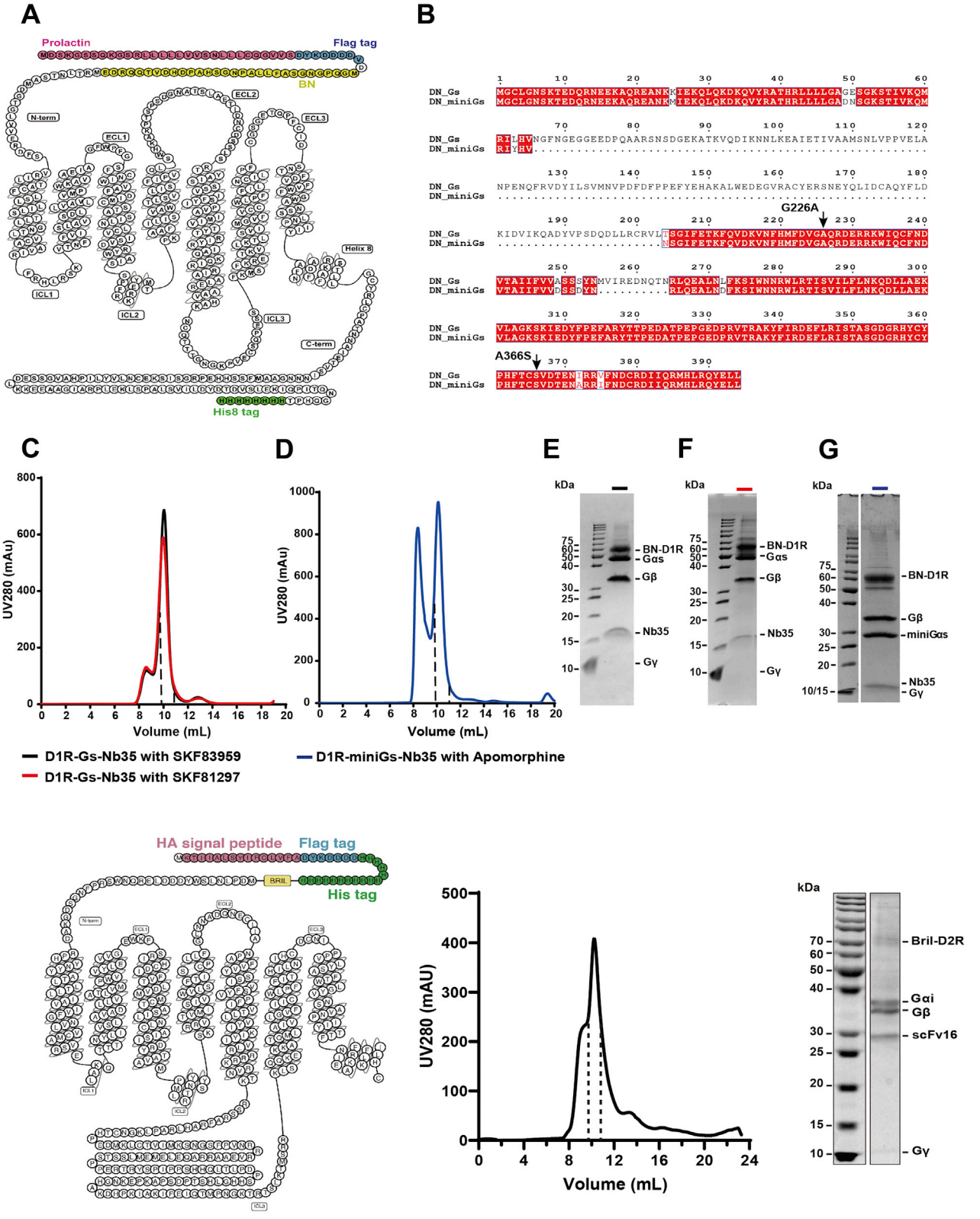

(legend on next page)

Figure S1. Constructs and purification of D1R-G_s-Nb35 complexes and D2R-bromocriptine-G_i-scFv16 complex, related to Figure 1

(A) Snake plot diagram of wild-type D1R construct used in this study. BN: β_2AR N-terminal tail region; Prolactin: prolactin precursor sequence.

(B) Sequence alignment of $G_{\alpha s}$ and engineered mini-$G_{\alpha s}$ used in this paper. The dominant-negative mutation sites were marked with black arrow.

(C-D) Size exclusion chromatography (SEC) profiles of D1R-G_s complexes bound with SKF81297, SKF83959 (C) and D1R-miniG_s complex bound with apomorphine (D).

(E-G) SDS-PAGE analysis of D1R-G_s in complex with SKF81297(E), SKF83959 (F) and hD1R-miniG_s in complex with apomorphine (G) after SEC separation.

(H) Snake plot diagram of wild-type D2R construct used in this study.

(I) Size exclusion chromatography (SEC) profiles and SDS-PAGE analysis of D2R-bromocriptine-G_i complex.

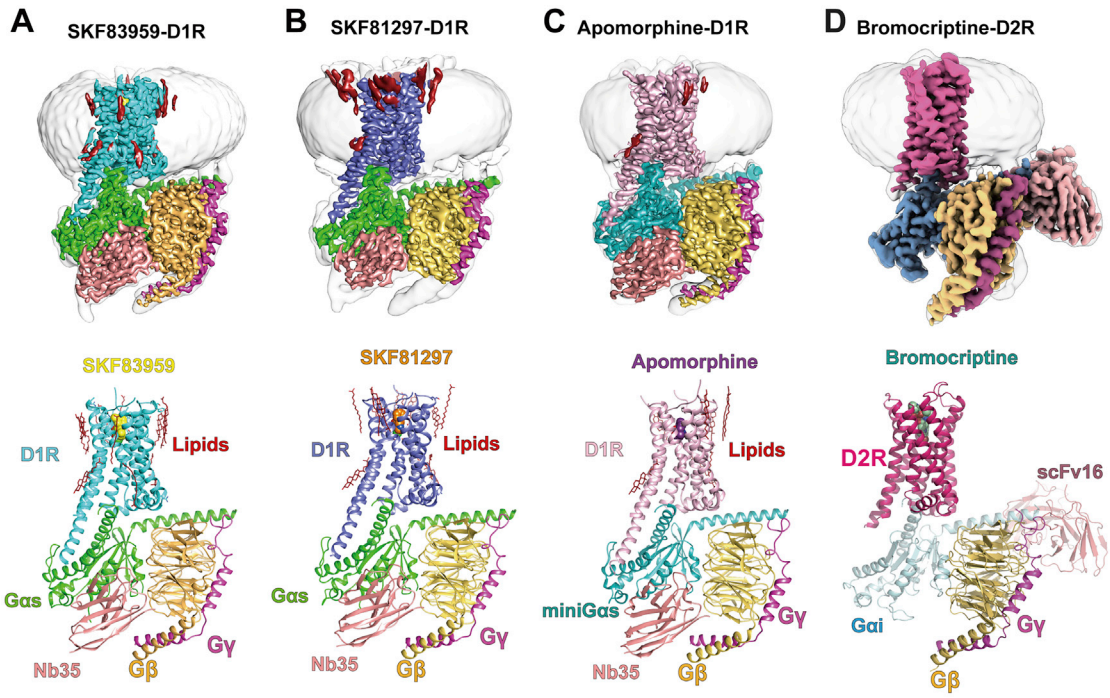

Figure S2. Cryo-EM structures of the SKF83959, SKF81297, and apomorphine-bound D1R-G_s complexes and bromocriptine-bound D2R-G_i complex, related to Figure 1

Cryo-EM density maps and models of the D1R-G_s complex with agonists SKF83959 (A) SKF81297 (B) and apomorphine (C), and wild-type hD2R-G_i complex with bromocriptine (D). The colored density map is shown at 0.035, 0.050, 0.054 threshold for SKF83959, SKF81297 and apomorphine-bound hD1R-G_s complexes, respectively. Color usage: SKF83959, yellow; SKF81297, orange; apomorphine, violet-purple; $G_{\alpha s}$, green; mini$G_{\alpha s}$, teal; G_β, yellow orange; G_γ, light magenta; Nb35, salmon; putative cholesterols and lipids, red; D1R is shown in cyan (SKF83959-bound complex), slate (SKF81297-bound complex) and light pink (apomorphine-bound complex), respectively. For D2R-bromocriptine-G_i-scFv16 complex, the density is shown at 0.025 threshold. Color usage: D2R: hot pink; bromocriptine: light green; $G_{\alpha i}$, pale cyan; G_β, yellow orange; G_γ, light magenta; scFv16: dark salmon.

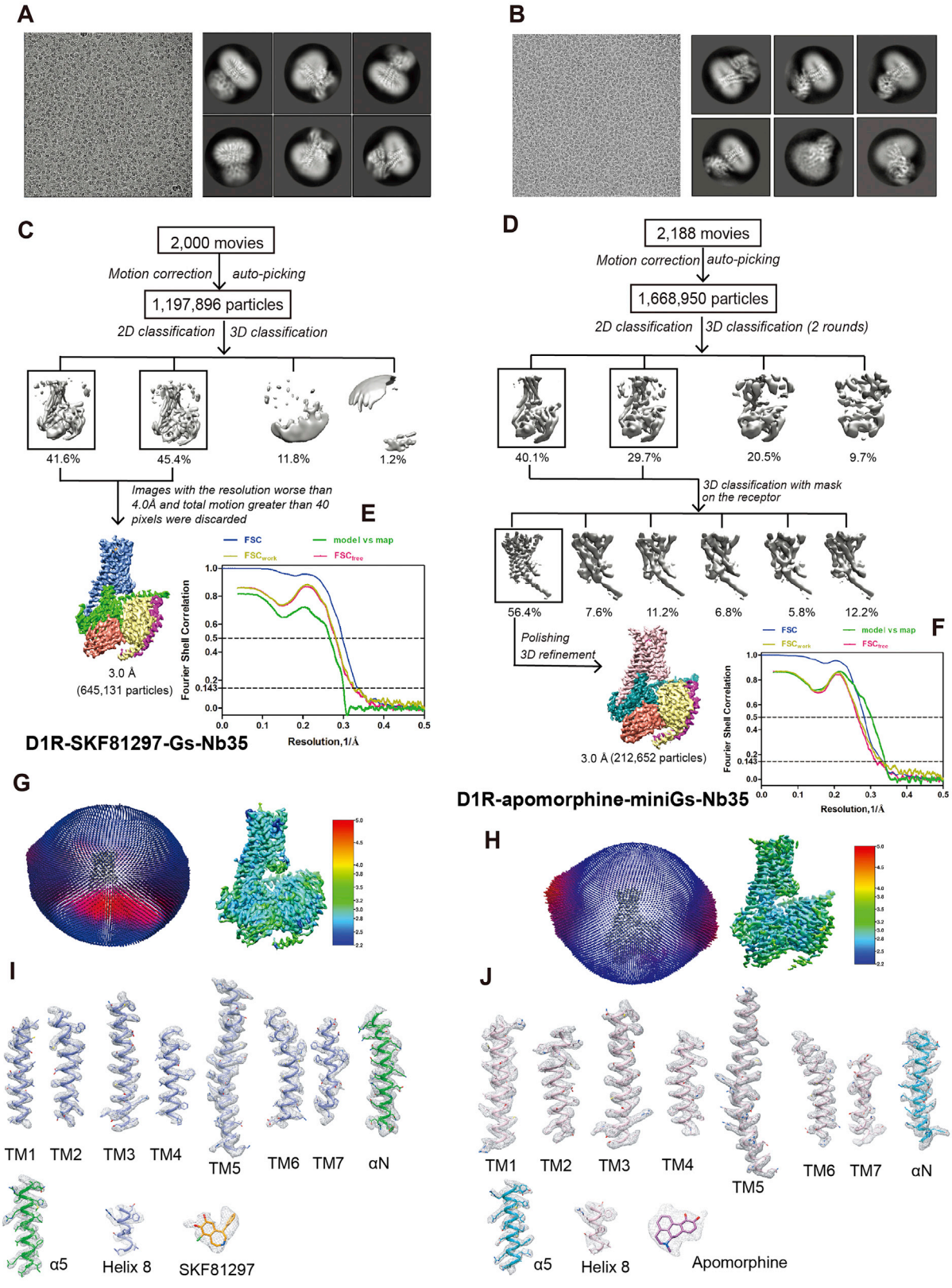

(legend on next page)

Figure S3. Single particle cryo-EM and structure determination of D1R-SKF81297-G_s and D1R-apomorphine-miniG_s, related to Figure 1

(A-B) Representative cryo-EM micrographs and 2D classification averages of D1R-SKF81297-G_s (A) and D1R-apomorphine-miniG_s (B).

(C-F) Cryo-EM data processing workflows of D1R-SKF81297-G_s (C) and D1R-apomorphine-miniG_s (D) by Relion 3.0, the 'Gold-standard' Fourier shell correlation (FSC) curves were placed at the right corner, with the global resolution defined at the FSC = 0.143 is 3.0Å for D1R-SKF81297-G_s (E) and 3.0Å for D1R-apomorphine-miniG_s (F).

(G-H) Angle distribution maps and cryo-EM maps of D1R-SKF81297-G_s (G) and D1R-apomorphine-miniG_s (H) colored by local resolution(Å). The density map is shown at 0.048 and 0.052 threshold for SKF81297 and apomorphine-bound complexes, respectively.

(I-J) Density maps of transmembrane helixes TM1-TM7 and helix 8 of D1R, αN and α5 helices of $G_{\alpha s}$/ mini$G_{\alpha s}$ and the ligand of D1R-G_s bound with SKF81297(I) and D1R-miniG_s bound with apomorphine (J). The cryo-EM density is shown at 0.048 and 0.052 threshold for SKF81297 and apomorphine-bound complexes, respectively.

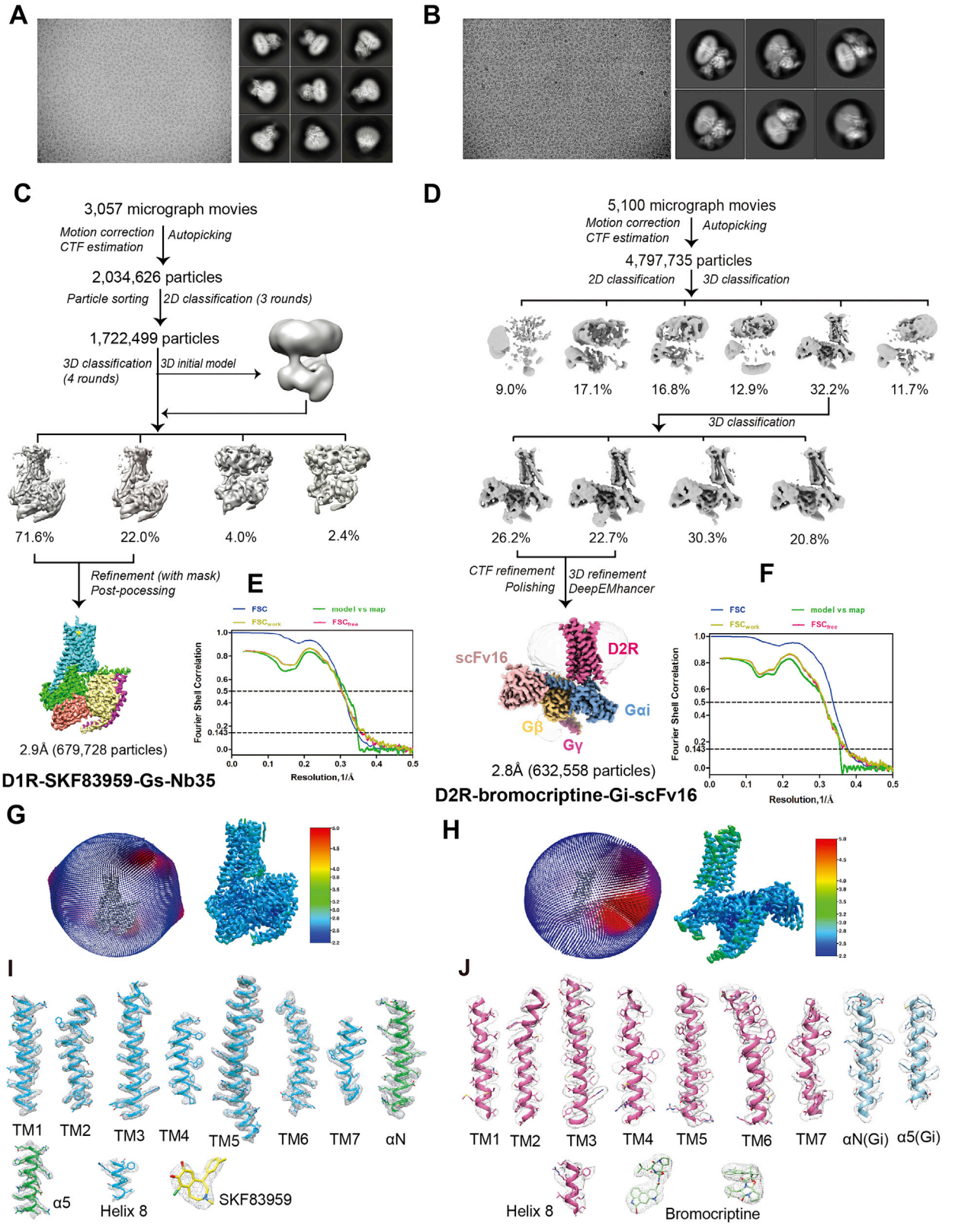

(legend on next page)

Figure S4. Single particle cryo-EM and structure determination of D1R-SKF83959-G_s and D2R-bromocriptine-G_i, related to Figure 1

(A-B) Representative cryo-EM micrographs and 2D classification averages of D1R-SKF83959-G_s (A) and D2R-bromocriptine-G_i (B).

(C-F) Cryo-EM data processing procedures of D1R-SKF83959-G_s (C) and D2R- bromocriptine-G_i (D) using Relion 3.0, the 'Gold-standard' Fourier shell correlation (FSC) curves were placed at the right corner, with the global resolution defined at the FSC = 0.143 is 2.9Å for D1R-SKF83959-G_s (E) and 2.8Å for D2R-bromocriptine-G_i (F).

(G-H) Angle distribution maps and cryo-EM map of D1R-SKF83959-G_s (G) and D2R- bromocriptine-G_i (H) colored by local resolution(Å). The density map is shown at 0.035 and 0.065 threshold for D1R-SKF83959-G_s complex and D2R- bromocriptine-G_i complex, respectively.

(I) Density maps of transmembrane helixes TM1-TM7 and helix 8 of D1R, αN and α5 helices of $G_{\alpha s}$ and the ligand of D1R-G_s bound with SKF83959. The cryo-EM density is shown at 0.032 threshold.

(J) Cryo-EM density maps of the transmembrane helixes 1-7 (TM1-TM7), the helix 8 (H8) of D2R; αN, α5 helices of $G_{\alpha i}$, and the ligand bromocriptine. The cryo-EM density is shown at 0.015 threshold.

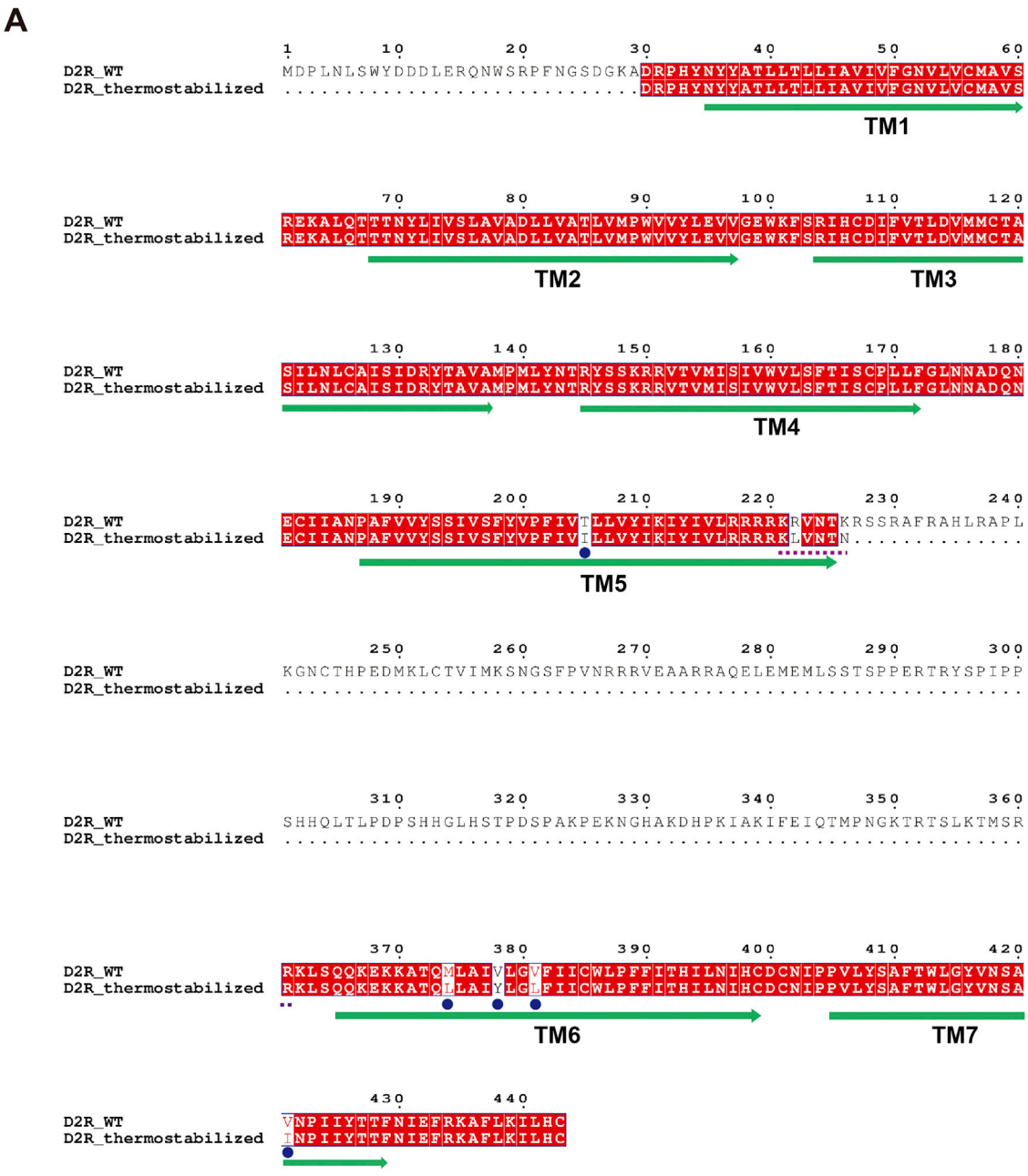

(legend on next page)

Figure S5. Sequence alignments, related to Figures 2 and 6D

(A) Sequence alignment of human wild-type D2R and thermostabilized D2R. Amino acid sequence alignment of wild-type D2R used in our study and the thermostabilized D2R in previously reported D2R-G_i structure (PDB: 6VMS). Each transmembrane helix was marked with green arrow. The mutation sites in thermostabilized D2R were marked with blue dots while the ICL3 linker in it was marked with purple dashed line.

(B) Sequence alignment of ECL2 region of dopamine receptors. The ECL2 sequences of D2R and D3R show large differences with other dopamine receptors, especially D1R and D5R.

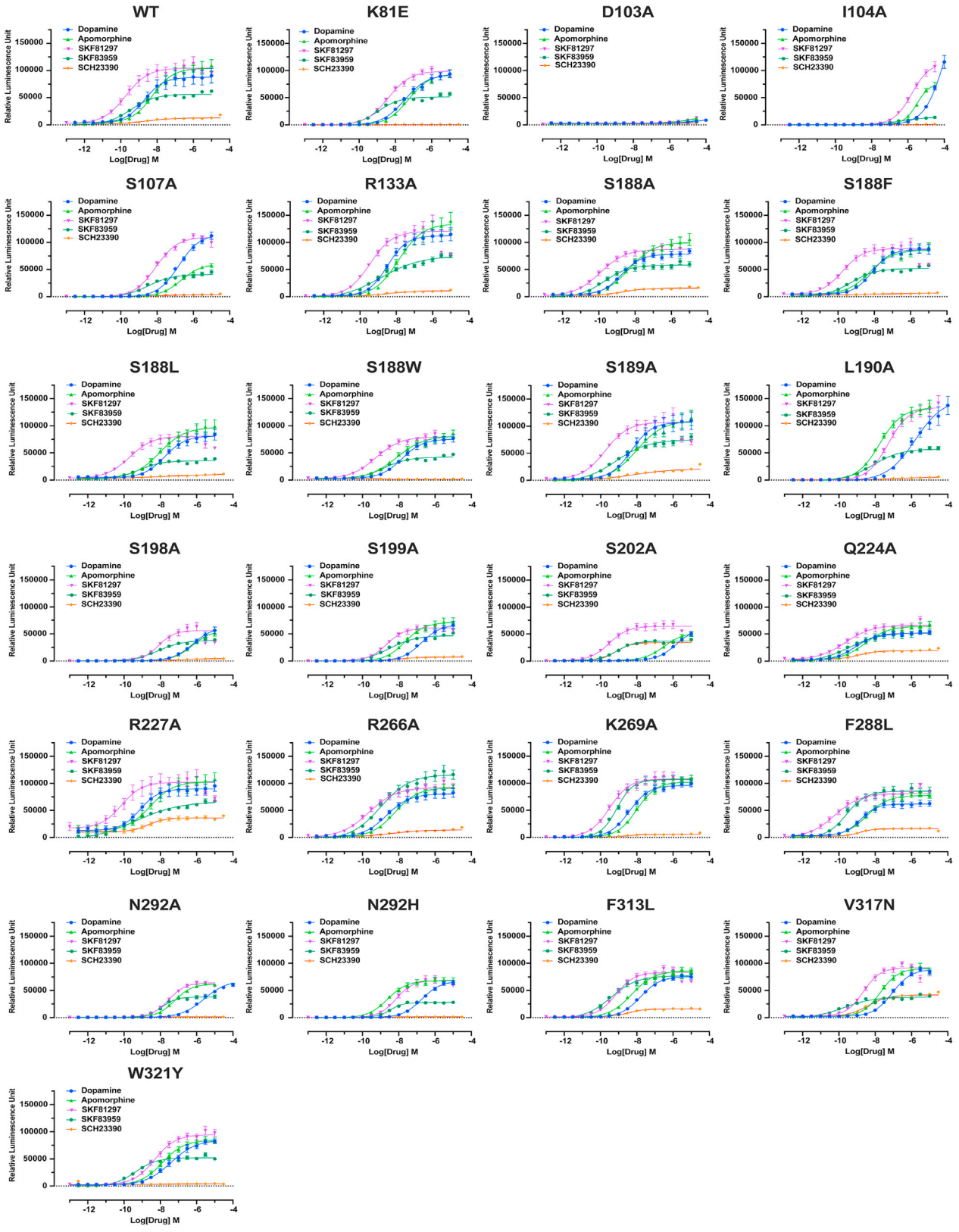

(legend on next page)

Figure S6. cAMP accumulation data of wild-type D1R and D1R mutants, related to Figure 3G and Table S4

Graphical representation of cAMP accumulation assay (Glosensor) data for identified D1R wild-type and mutants. x axis values are displayed as the Logarithm (Log_{10}) concentration of the respective drug. y axis values are displayed as the average Relative Luminescence Unit (RLU) values obtained from TriLux Microbeta plate counter for each assay. Dose response curves were further analyzed using ''log(agonist) vs. response – Variable slope (four parameters)'' function in Graphpad Prism 8.4 software (Graphpad Software Inc., San Diego, CA). All data are presented as mean values ± standard error of measurement (SEM) with a minimum of four technical replicates and n = 3 biological replicates.

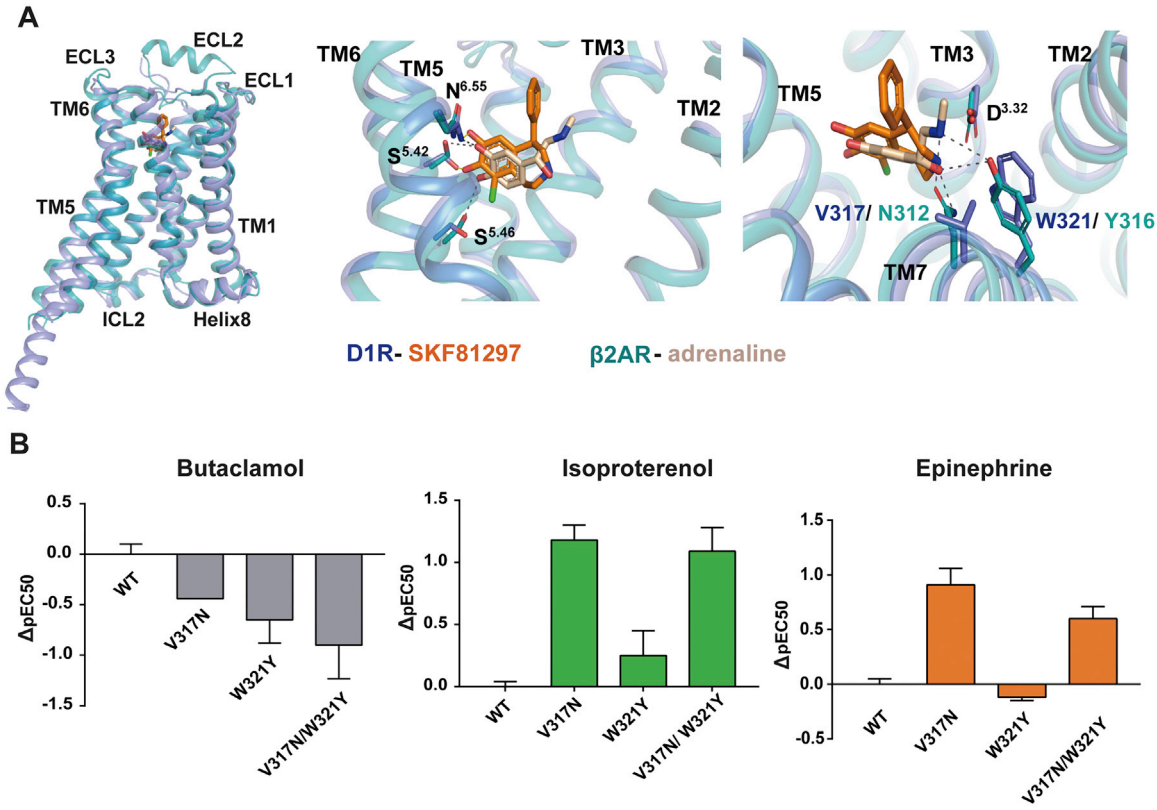

Figure S7. Analysis of D1R and β2AR in neurotransmitter recognition and specificity, related to Figure 4 and Table S5

(A) Structure alignment of D1R-SKF81297 and β_2AR-adrenaline. The hydrogen bonds between D1R and SKF81297 are marked with yellow dashed lines while the hydrogen bonds between β_2AR and adrenaline are marked with black dashed lines.

(B) cAMP accumulation data of wild-type D1R and D1R mutants activated by Butaclamol, ISO and EP. Butaclamol is included as a negative control, since it is a potent D1R antagonist. The data are shown as Δ pEC_{50}, relative to pEC_{50} of wild type. Results of F-test for Isoproterenol are $F(V317N)_{2,283} = 61.06$, $p < 0.0001$, $F(W321Y)_{2,283} = 2.234$, $p = 0.1090$, $F(V317N/W321Y)_{2,275} = 27.44$, $p < 0.0001$; Epinephrine are $F(V317N)_{2,277} = 106.5$, $p < 0.0001$, $F(W321Y)_{2,277} = 3.355$, $p = 0.0363$, $F(V317N/W321Y)_{2,382} = 3.633$, $p = 0.0273$.